Politecnico
di Torino
1859

Harvard John A. Paulson
School of Engineering
and Applied Sciences

EPFL

Grenoble INP
phelma

Sofia Cerasi

Wearable ultrasound sensors for assessing skeletal muscle kinematics: development and evaluation

Master Thesis

Politecnico di Torino

Supervisor

Elizabeth Suitor
Prof. Dr. Matteo Cocuzza
February 2023 - August 2023

Contents

Abstract **2**

Nomenclature **3**

1 Introduction **4**

2 Literature review **5**
- 2.1 Ultrasound physics 5
- 2.2 Ultrasound transducer 6
  - 2.2.1 Type of ultrasound transducer 7
- 2.3 Ultrasound imaging 9
  - 2.3.1 Basic principle 9
  - 2.3.2 Imaging modes 10

3 Single element ultrasound transducer **13**
- 3.1 Structure of a single element transducer 13
  - 3.1.1 Piezoelectric effect and material properties 16
- 3.2 Design of a single element transducer 19
  - 3.2.1 Electrical circuit model 20
  - 3.2.2 Finite element model 32
  - 3.2.3 KLM vs FEM 38
  - 3.2.4 Conclusions 39

4 Evaluation of muscle velocity **40**
- 4.1 Introduction 40
- 4.2 Literature review 41
  - 4.2.1 Velocity and strain measuring methods 41
  - 4.2.2 Ground truth 42
- 4.3 Muscle mimicking material 45
  - 4.3.1 Acoustic properties 45
  - 4.3.2 Fabrication process 47
  - 4.3.3 Results 51
- 4.4 Optical flow 62
  - 4.4.1 Implementing sparse optical flow 63
- 4.5 Doppler ultrasound method 65
- 4.6 Doppler vs Optical Flow 66

5 Conclusions **67**

Abstract

This thesis provides a comprehensive exploration into the evaluation of muscle velocity and the intricate design and optimization of ultrasound transducers. The research emphasizes the significance of Single Element Transducers (SET) for wearable applications, highlighting their advantages. Delving deeper into the transducer design, the study meticulously examines the structure and functionality of its components. By employing an electrical circuit model and a finite element model, the research achieves a harmonious blend of computational efficiency and design precision, ensuring the transducer's optimal performance. The thesis further explores muscle velocity evaluation methodologies, including Optical Flow and the Doppler Ultrasound method. It emphasizes the intricacies of velocity-measuring techniques and the essential need for an accurate ground truth. To cater to this need, the research delves into the fabrication of a phantom.

Nomenclature

Symbols

A	Area
ρ	Density
c	Longitudinal speed of sound
α	Acoustic attenuation factor
β	Real wave number
k	Complex wave number
γ_s	Structural loss factor
Z	Acoustic impedance
T	Acoustic intensity transmission coefficient
Q	Piezoelectric mechanical quality factor
${c_{33}}^D, {h_{33}}^D, {e_{33}}^S$	Stress-voltage piezoelectric constants in axial direction

Acronyms and Abbreviations

AAO Epoxy	Anodic Aluminum Oxide Epoxy
BSC	Backscatter Coefficient
FEM	Finite Element Model
FML	First Matching Layer
MMM	Muscle Mimicking Material
MTU	Muscle Tendon Unit
ROI	Region Of Interest
SET	Single Element Transducer
SML	Second Matching Layer
TMM	Tissue Mimicking Material
TL	Transmission Line

Chapter 1

Introduction

The integration of engineering and wearable technology has opened new frontiers for continuous, non-invasive health monitoring and intervention. Among these innovative solutions, wearable ultrasound sensors [1] [2] have the potential to revolutionize our understanding of human physiology, specifically skeletal muscle kinematics. However, traditional ultrasound systems suffer from inherent challenges such as large size, complexity, and high cost of production.

The focus of this thesis is twofold. Firstly, it aims to reduce the dimension and complexity of the transducer used in the ultrasound system, making it more portable, cost-effective, and easy to manufacture. This in turn could lead to wider adoption, increased accessibility, and greater potential for continuous monitoring. Secondly, it investigates strategies to accurately measure the velocity of skeletal muscles with less computational load, opening up the possibility of near real-time monitoring and analysis.

The skeletal muscle system plays a crucial role in human motor function. Its complex biomechanics, which involves the simultaneous coordination of numerous individual muscles, each with its unique properties and functions, has fascinated researchers for years. The velocity and strain of skeletal muscles are critical metrics for understanding muscle performance, physical health, and to detect anomalies indicative of various muscular disorders. However, existing methods to measure these parameters are computationally expensive [3] [4] [5], limiting their use in real-time applications and scenarios with constrained computational resources.

The importance of this research lies in its potential contribution to preventative healthcare, rehabilitation, sports science, and more. Beyond this, it holds the promise of equipping researchers and healthcare professionals with groundbreaking insights into muscle behavior. This could serve as a foundation for the development of novel treatments and interventions.

In the pursuit of pushing the boundaries of wearable health technology, this thesis blends design techniques, engineering principles, and comprehensive experimentation. The ensuing discussions and analyses unravel how a new generation of wearable ultrasound sensors for skeletal muscle kinematics measurement can be achieved, ultimately leading us a step closer to a future where high-quality healthcare is affordable, accessible, and seamlessly integrated into our daily lives.

Chapter 2

Literature review

An ultrasound system typically comprises three fundamental components: the transducer probe, the computer unit, and a monitor display as it is possible to see in Figure 2.1. The underlying principle of ultrasound operation revolves around the transducer probe's ability to emit and capture ultrasound signals, subsequently transforming them into voltage readings. These voltage readings are then processed by the computer, meticulously translating them into a coherent and visually discernible image displayed on the monitor for the user's observation.

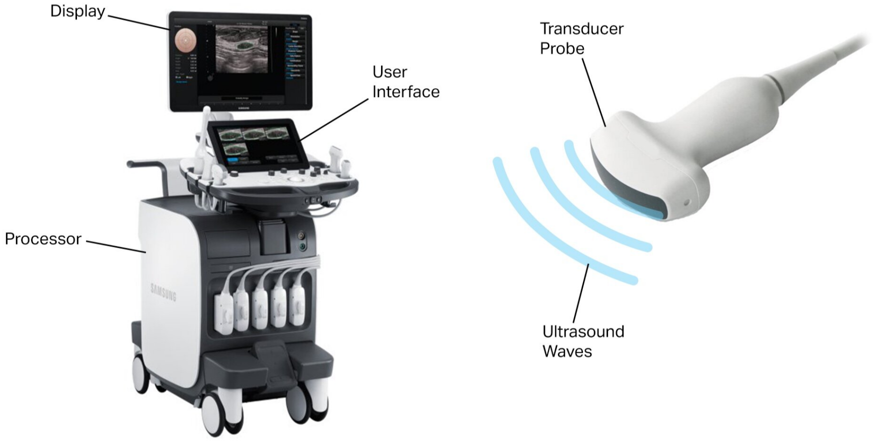

Figure 2.1: Typical ultrasound system. Image by [6]

2.1 Ultrasound physics

Ultrasound technology is an integral part of various scientific and technological fields, notably in healthcare, where it is a non-invasive tool used for imaging and diagnosis. The term 'ultrasound' refers to sound waves with frequencies above the range of human hearing, typically above 20 kHz. It is the fundamental physics of these sound waves that allows us to harness their properties and apply them to a multitude of uses, including the focus of this thesis, wearable sensors.

Sound is a mechanical wave phenomenon, resulting from the vibration of particles in a medium, such as air, water, or biological tissue. Like any wave, ultrasound waves have properties of wavelength, frequency, velocity, and amplitude. Frequency refers to the number of cycles a wave completes in a second, and for ultrasound, this is

typically in the range of 1 MHz to 15 MHz for medical applications. Wavelength is the distance over which one cycle of the wave occurs, and it depends on both the frequency and the speed of sound in the medium. The velocity of sound is a characteristic of the medium and depends on its density and elasticity.
Ultrasound waves propagate through a medium until they encounter a boundary with a different medium. At this point, they can be reflected, refracted following Snell's law, or absorbed, all of which are critical to the functioning of ultrasound technologies. Reflection occurs when the wave bounces back from the boundary, refracted waves are those that change direction as they pass into the new medium, and absorption is the conversion of the wave's energy into heat. The three different behaviors are shown in Figure 2.2.

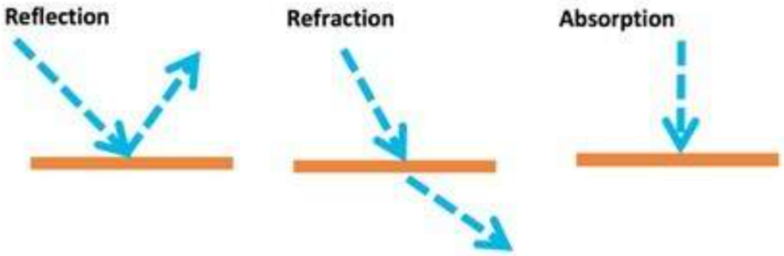

Figure 2.2: Behavior of the sound wave when it encounters a different medium. Image by [7]

The principle behind ultrasound imaging and sensing, including wearable sensors, lies in these interactions. When an ultrasound wave encounters a boundary between different tissues or materials, some of the wave's energy is reflected back. By detecting and analyzing these reflected signals, it's possible to create images or gather information about the structure and composition of the material or tissue.
One of the key components of any ultrasound system is the transducer, which characterizes both the transmitter and receiver of ultrasound waves. It converts electrical energy into mechanical energy, producing ultrasound waves, and the reverse process is also possible to detect the reflected waves.

2.2 Ultrasound transducer

Ultrasound sensors come in various forms and have multiple settings that can be adjusted to modify the type of sound wave they generate. In the majority of ultrasound systems, piezoelectric materials are employed in the sensor components. This kind of material has the ability to transform mechanical stress into electrical energy, a phenomenon known as the piezoelectric effect. This process is bidirectional: applying an electric charge will make the material oscillate. Factors such as the oscillation rate of the materials, the distance between each oscillating unit, the sampling rate of incoming sound, and the layout and shape of the oscillating units significantly influence the emitted sound wave.

2.2.1 Type of ultrasound transducer

Ultrasound transducers can be found in diverse shapes and sizes in order to cater to the specific requirements of the diagnostic medical sonographer. Figure 2.3 shows the common ultrasound probes, featuring, from left to right, a curvilinear, a linear, and a phased array transducer with the relative type of ultrasound image that are able to picture.

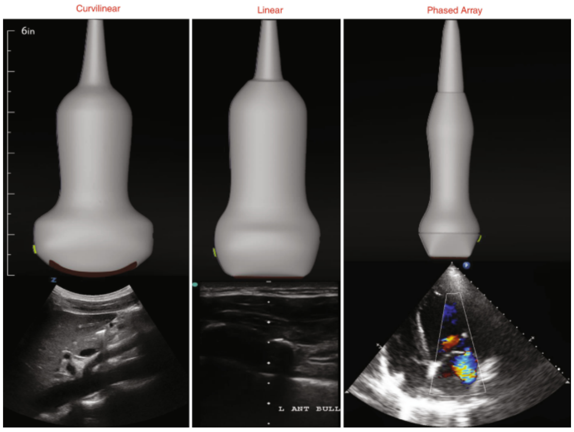

Figure 2.3: Types of ultrasound transducer and relative ultrasound image. Image by [8]

Transducer types not only vary in the shape of the ultrasound image they produce but also in the range of frequencies they can deliver [9]. For instance, a curvilinear transducer operates at a relatively low frequency, enabling sound waves to penetrate deeply into the body and reveal structures as deep as 25 cm or more. This characteristic is beneficial for capturing details from deeper regions since low-frequency waves possess excellent penetration capabilities. However, this advantage comes at the cost of overall resolution, as the display of finer details may be somewhat limited compared to a linear transducer.

On the other hand, the linear transducer employs a higher frequency, allowing it to penetrate only a few centimeters. Consequently, it excels at creating exceptional images in the near-field, providing clearer details for structures closer to the transducer's surface. Moreover, the high-frequency nature of the linear transducer grants it a remarkable temporal resolution, making it suitable for visualizing blood flow in slow-moving vessels.

As for the phased array probe, its frequency lies somewhere between the curvilinear and linear probes. It offers a narrower sector compared to the curvilinear probe, conserving computing power while simultaneously enhancing temporal resolution and imaging depth compared to the linear probe. These advantages prove crucial in examining organs that are both large and fast-moving, such as the heart, where imaging depth and temporal resolution play significant roles in obtaining accurate and detailed results.

The primary drawback associated with the three types of ultrasound transducers mentioned lies in their inherent complexity. This complexity makes them less desirable for integration into wearable sensors. Indeed, when it comes to wearable sensor applications, the optimal choice for an ultrasound transducer is a single-element variant.

Single element transducer

The single-element transducer represents the most fundamental and straightforward design among ultrasound transducers. It consists of a single piezoelectric crystal that functions as both the transmitter and receiver of ultrasound waves. This simplicity allows for cost-effective manufacturing, making single-element transducers accessible and widely used in various basic ultrasound applications.

Compared to more advanced transducer types like phased array, linear, and curvilinear transducers, single-element transducers have certain limitations. One significant drawback is their lack of electronic steering capabilities. Unlike phased array transducers that can electronically manipulate the beam direction or linear and curvilinear transducers that offer specific beam shapes, single-element transducers produce a fixed and unfocused ultrasound beam. This restricts their ability to target specific structures or perform real-time adjustments during imaging. The fixed and unfocused beam of single-element transducers can result in limited image resolution at shallower depths.

In summary, single-element transducers are a basic and cost-effective option for imaging deep structures where fine resolution is less critical. While they lack the advanced capabilities of other transducer types like electronic steering and high-resolution imaging, they still serve a vital role in specific ultrasound applications that demand deep penetration.

2.3 Ultrasound imaging

Ultrasound imaging is a non-invasive and widely used medical imaging technique that allows visualization of internal body structures [10]. This technology relies on the principles of sound waves and their interactions with tissues to generate detailed images of organs and tissues. Different imaging modes, such as A-mode, B-mode, and Doppler [11], further enhance the capabilities of ultrasound imaging, offering valuable insights into tissue characteristics, blood flow, and anatomical details. In the following sections, we will explore these different ultrasound imaging modes and their applications in medical practice.

2.3.1 Basic principle

At the core of ultrasound imaging is the ultrasonic transducer. The transducer emits a focused beam of ultrasound into the area of interest within the subject. When the ultrasound encounters an acoustic boundary, within the tissue, some of the energy is reflected back towards the transducer.

Upon reaching the transducer, the returning echoes interact with the piezoelectric crystal within the transducer, generating electric signals. These signals are then electronically processed and measured, allowing the location of the echo's origin to be precisely determined.

Ultrasonic imaging involves mapping the patterns of echoes reflected from acoustic boundaries within tissues as shown in Figure 2.4. Different tissues exhibit characteristic echo patterns, enabling the differentiation of structures in the image. The fundamental diagnostic parameters extracted from ultrasound imaging are the size of an echo and the distance of its origin from the transducer.

To construct the ultrasound image, the ultrasound beam is systematically scanned across the subject. For each position of the beam, a set of signals is recorded along its path, representing reflections from boundaries at various distances. These sets of signals, often referred to as "scan lines", provide one-dimensional information along the beam path. By sweeping the ultrasound beam across the subject in a chosen direction, multiple scan lines are generated, creating a two-dimensional (2-D) image of a plane within the subject. [13]

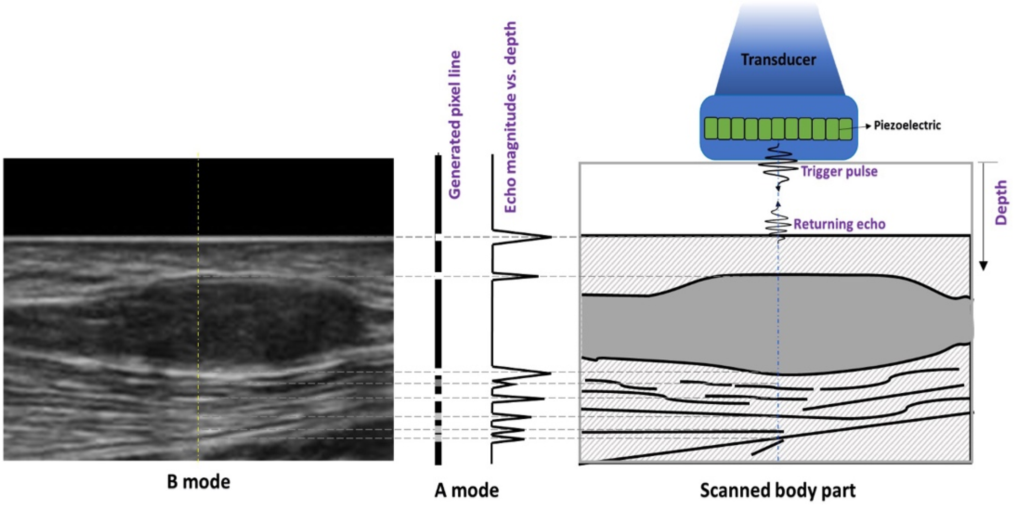

Figure 2.4: Ultrasound imaging as patter of echoes. Image by [12]

2.3.2 Imaging modes

Ultrasound imaging has transformed medical diagnostics, offering non-invasive visualization of internal structures in real-time. Modern ultrasound systems come with a range of imaging modes, each serving specific clinical applications. This discussion explores the basic principles of ultrasound imaging and delves into the principal imaging modes such as A-mode, B-mode, and Doppler-mode.

A-mode

A-mode, also known as Amplitude Mode, stands as one of the earliest iterations of ultrasound imaging. Within A-mode, it was possible to gauge the separation between tissues. The depiction in Figure 2.5 exemplifies A-mode, where peaks on the graph below the illustration symbolize ultrasound echoes sent back by tissue interfaces. With the passage of time, the amplitude of each returning echo diminishes due to ultrasound attenuation.
While A-mode has been outpaced by newer scanning modes in contemporary ultrasound systems, it set the groundwork for the evolution of the more prevalent ultrasound modes in use today.

B-mode

B-mode, also known as Brightness mode, translates the amplitude peaks identified in A-mode into pixels that exhibit varying levels of brightness as can be seen in Figure 2.6. This method provides a more intuitive portrayal of ultrasound data.

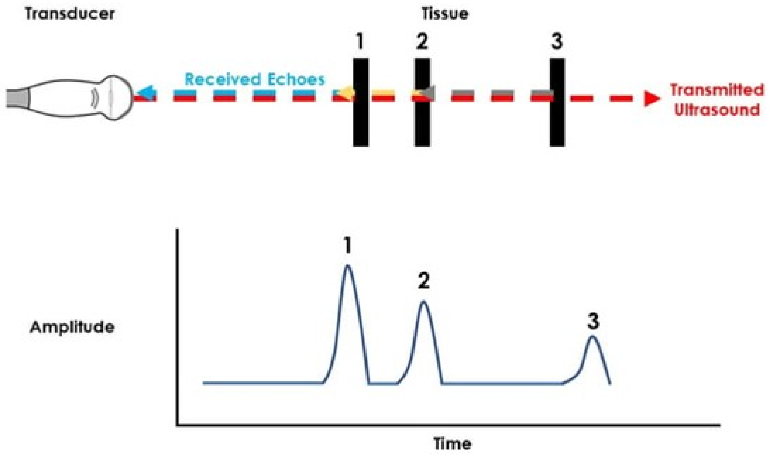

Figure 2.5: A-mode imaging principle. Image by [11]

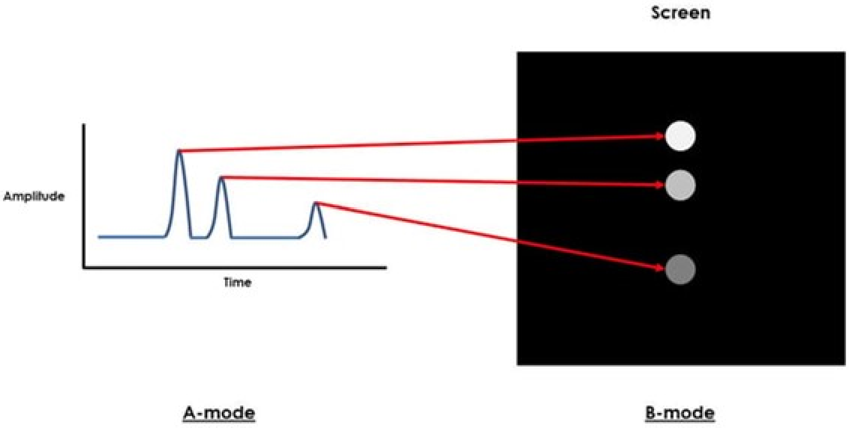

Figure 2.6: Visual transformation from A-mode to B-mode. Image by [11]

Within the A-mode, amplitude traces are displayed linearly, as exemplified on the left-hand side of Figure 2.6. In the B-mode, each of these amplitude peaks is translated into pixels exhibiting varying shades of gray. The level of brightness in each pixel corresponds to the amplitude of the echo sent back to the transducer. Additionally, the pixel's location on the screen is influenced by the time it takes for each echo to return, thus reflecting the depth of the structure within the subject being examined.

By employing the B-mode approach, ultrasound systems can emit consecutive ultrasound pulses in multiple directions, facilitating the creation of multiple image lines. This procedure occurs rapidly and is repeated continuously, ultimately producing the familiar real-time ultrasound image commonly observed on various ultrasound systems.

Doppler-mode

Most modern ultrasound systems possess the capability to utilize the Doppler effect, a phenomenon that involves frequency changes when ultrasound waves interact with moving objects. This feature facilitates the measurement of a moving subject's direction and velocity, providing crucial information across multiple clinical scenarios.
Broadly, there are two fundamental approaches for visually displaying Doppler data. The two principal methods are the following:

- Spectral Doppler: This display provides a graphical representation of velocities over time, which is often presented as a waveform as it can be seen in Figure 2.7 on the bottom. It can provide quantitative information, such as peak or mean velocities, which can be used for diagnosis and assessment of conditions such as valvular heart disease or vascular stenosis.

- Color Doppler: This tool superimposes color onto the B-mode image to represent flow as shown in Figure 2.7. Different colors represent the direction of flow relative to the transducer (typically red for flow towards, and blue for flow away from the transducer), and the color intensity reflects the velocity of the flow.

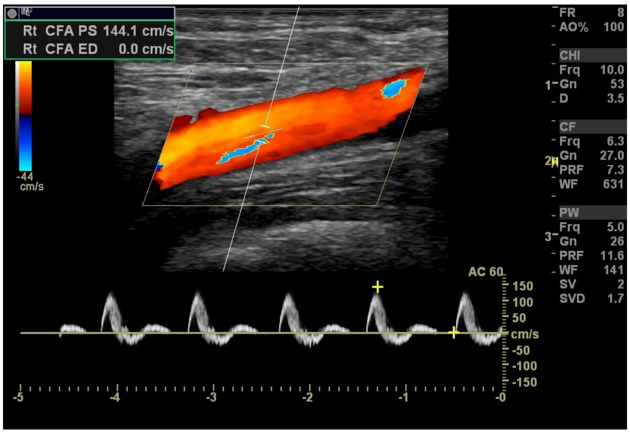

Figure 2.7: Types of Doppler mode imagining. Image by [14]

Chapter 3

Single element ultrasound transducer

Curvilinear, array, and linear transducers each have their specific applications in diagnostic and imaging processes. However, wearable ultrasound sensors require the use of a Single Element Transducer (SET) as they offer distinct advantages for wearable applications. Their simplified design reduces the complexity inherent in multi-element transducers. This not only translates to a reduction in power consumption, a crucial factor for wearable sensors, but also provides a more consistent response over the entire sensing area. Multi-element transducers can occasionally struggle with uniform sensitivity across all elements, whereas a SET, by its very design, avoids this problem.

However, designing an efficient SET is not without its challenges. To achieve optimal performance, understanding the device's electrical behavior is pivotal. This chapter delves deep into the exploration of an equivalent electrical circuit of SET, which has been studied to decipher the principal parameters that drive maximum efficiency. Following this, we leverage the capabilities of COMSOL Multiphysics simulations, providing insights into the finer nuances of the transducer design, and ensuring its optimization.

3.1 Structure of a single element transducer

A transducer is a device that converts one form of energy into another. Within the realm of wearable ultrasound transducers, this component alters electrical energy into mechanical energy and conversely, converting between the two types of energy. In its simplest form, a single-element transducer consists of a piezoelectric element and a matching layer, along with other components like backing material and an acoustic lens as it is possible to see in Figure 3.1.

Following is a concise breakdown of the structure and functionality of each of these components [16]:

- **Piezoelectric Element**
  The piezoelectric element is the heart of the ultrasound transducer. It is typically made from a ceramic material like lead zirconate titanate (PZT). When an electric field is applied to the material, it changes shape, producing mechanical pressure waves (sound). Conversely, when the material is exposed

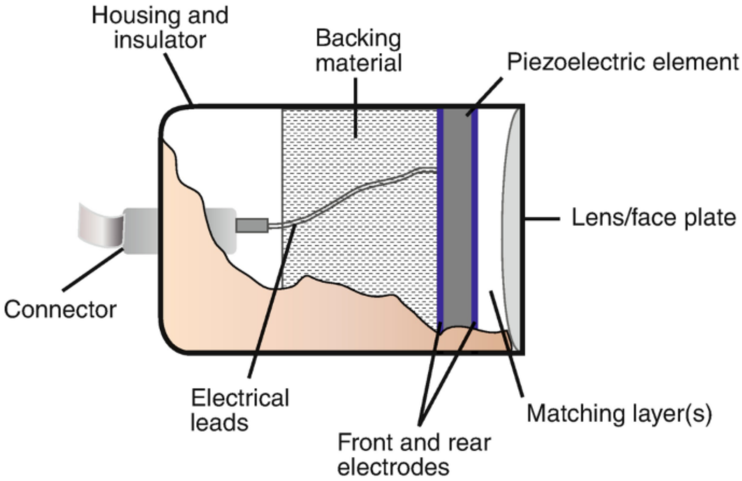

Figure 3.1: Structure of a single element transducer. Image by [15]

to pressure waves, it generates an electric field. This property allows the piezoelectric element to act as both a transmitter and a receiver of ultrasound waves.

- **Matching Layer**
  The matching layer is positioned between the piezoelectric element and the patient's body. Its primary function is to mitigate the impedance mismatch that exists between the piezoelectric element and the medium (body). This reduction in mismatch helps to minimize the reflection that occurs at the interface, thereby facilitating a more efficient transmission of ultrasound waves into the tissue. Without a matching layer, a major fraction of the ultrasound waves would reflect back toward the transducer. This behavior can be quantified using the reflection coefficient, represented as:

$$R = \frac{Z_2 - Z_1}{Z_2 + Z_1} \tag{3.1}$$

  Here, Z_2 represents the acoustic impedance of the material into which the wave intends to propagate, and Z_1 denotes the acoustic impedance of the material from which the wave is coming from. To mitigate these reflections, the matching layer is typically constructed from a material whose acoustic impedance lies between the values of the piezoelectric material and the human body's tissue as will be shown later. This intermediary impedance ensures a smoother transition, reducing reflections and enhancing transmission efficiency.

- **Backing Material**
  Frequently denoted as the damping material, the backing layer is situated at the rear of the piezoelectric component. Its primary role involves absorbing ultrasound waves that travel in the opposite direction of the medium (body), effectively preventing any interference with the intended sound capture. Moreover, the backing material serves to attenuate the resonant vibrations within the piezoelectric element. As a result, this action contributes to an enhancement in axial resolution and a broader bandwidth, both of which are valuable attributes for ultrasound imaging.

- **Electrodes**
  These are thin conductive layers on the front and back surfaces of the piezoelectric material. They allow the application of an electric field across the piezoelectric material and also capture the electric field produced when the material is exposed to ultrasound waves.

- **Casing**
  The entire assembly is enclosed in a casing that protects the internal components from physical damage and insulates the patient from electrical exposure.

In operation, the transducer is coupled to the patient's body using an ultrasound gel whose role is crucial. Indeed, the ultrasound gel allows to diminish the formation of air gaps at the interface between the transducer and the medium. These gaps, if left unaddressed, can significantly compromise the transducer's performance by amplifying energy reflection and introducing distortions in the transmitted waves. A visual depiction of this concept is provided in Figure 3.2.

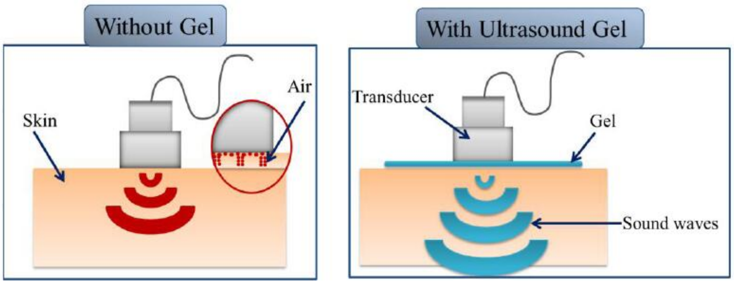

Figure 3.2: Ultrasound wave transmission with and without the use of ultrasound gel. Image by [17]

3.1.1 Piezoelectric effect and material properties

The piezoelectric effect is fundamental to the functioning of piezoelectric ultrasound transducers. This property allows specific materials to convert an applied mechanical strain into electric charges on their surfaces and vice versa. These transformations are key to the generation and reception of sound waves in ultrasound systems. By modulating the voltage frequency applied to a piezoelectric material, we can control its vibration to produce sound waves at that frequency. These waves then traverse through a medium, bouncing off objects or boundaries present, and return to the transducer. The transducer, utilizing the direct piezoelectric effect, converts the received acoustic energy back into electrical charges for interpretation by the ultrasound system's central processing unit. The direct and inverse piezoelectric effects are illustrated in Figure 3.3

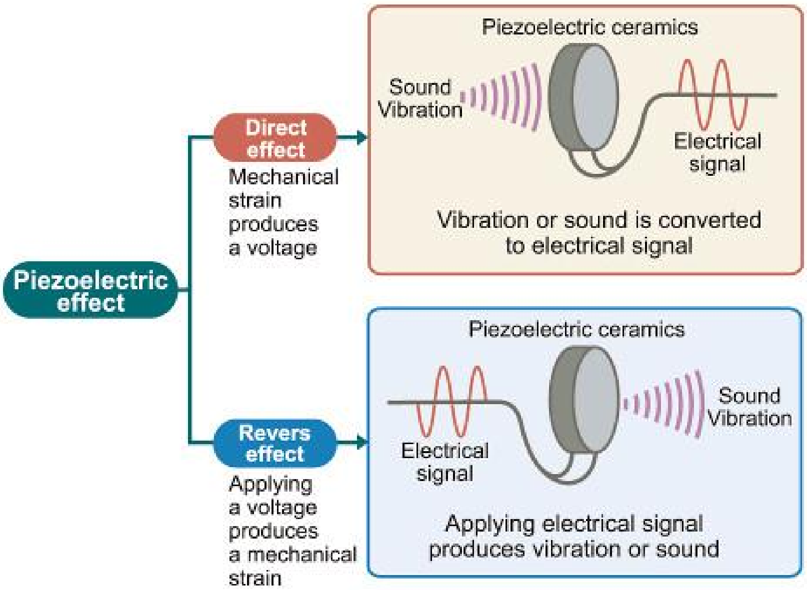

Figure 3.3: Visualization of the piezoelectric effect. Image by [18]

Piezoelectric materials showcase distinct characteristics, as illustrated by particular coefficients, and these properties can vary across different axes inside the material, symbolized by subscripts ij. Here's a breakdown of these features:

- **Piezoelectric Charge Coefficient - d** It indicates the level of polarization that arises from a unit of mechanical stress (T) exerted on the piezoelectric substance. Conversely, it signifies the mechanical deformation (S) the material undergoes when an electric field is applied.

- **Piezoelectric Voltage Coefficient - g** This descriptor illuminates the electric field that a piezoelectric material generates in response to each unit of mechanical stress. Alternatively, it indicates the mechanical deformation the material faces when an electric displacement is employed.

- **Dielectric Response - ϵ** It elucidates a material's reaction to the influence of an electric field. It measures the tendency or alignment of the electrical charges inside the material when exposed to a standardized electric field.

- **Electromechanical Conversion Efficiency - k** This parameter highlights the prowess of a piezoelectric material in transitioning electrical energy into its mechanical counterpart, or the reverse. It encapsulates the material's proficiency in alternating between these energy modalities.

Furthermore, piezoelectric materials can be characterized by several forms of impedance, reflecting their multifaceted interactions:

- **Acoustic impedance**
  It characterizes a material's resistance to the propagation of sound waves. It's calculated by multiplying the density of the material ρ by the speed of sound within that material (c), given by $Z_a = \rho c$

- **Electrical impedance**
  It defines the material's resistance to electrical flow when a voltage is applied.

- **Mechanical Impedance**
  It refers to the resistance a material offers to motion when subjected to a mechanical force. This property dictates how vibratory energy is transferred or absorbed.

- **Electromechanical Impedance**
  It describes the efficiency with which electrical energy is converted to mechanical energy and vice versa. The coupling coefficient is a measure of this impedance.

A summary of these properties and more for the main piezoelectric materials are shown in Figure 3.4.
Piezoelectric materials are chosen based on the specific needs of an application, and they fall into four main categories: single crystals, ceramics, polymers, and composites. Among ceramics, materials like lead zirconate titanate (PZT) stand out due to their efficient energy conversion, evidenced by their high electromechanical coupling

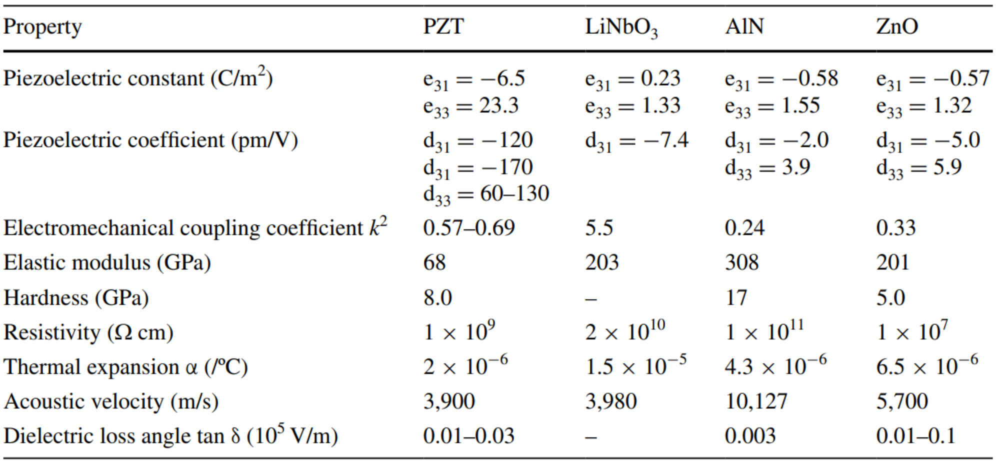

Property	PZT	$LiNbO_3$	AlN	ZnO
Piezoelectric constant (C/m^2)	$e_{31} = -6.5$ $e_{33} = 23.3$	$e_{31} = 0.23$ $e_{33} = 1.33$	$e_{31} = -0.58$ $e_{33} = 1.55$	$e_{31} = -0.57$ $e_{33} = 1.32$
Piezoelectric coefficient (pm/V)	$d_{31} = -120$ $d_{31} = -170$ $d_{33} = 60$–130	$d_{31} = -7.4$	$d_{31} = -2.0$ $d_{33} = 3.9$	$d_{31} = -5.0$ $d_{33} = 5.9$
Electromechanical coupling coefficient k^2	0.57–0.69	5.5	0.24	0.33
Elastic modulus (GPa)	68	203	308	201
Hardness (GPa)	8.0	–	17	5.0
Resistivity (Ω cm)	1×10^{9}	2×10^{10}	1×10^{11}	1×10^{7}
Thermal expansion α (/°C)	2×10^{-6}	1.5×10^{-5}	4.3×10^{-6}	6.5×10^{-6}
Acoustic velocity (m/s)	3,900	3,980	10,127	5,700
Dielectric loss angle tan δ (10^5 V/m)	0.01–0.03	–	0.003	0.01–0.1

Figure 3.4: The table presents the primary piezoelectric properties and parameters for four common piezoelectric materials: PZT, $LiNbO_3$, AlN, and ZnO. Table by [19]

coefficients. These coefficients indicate the material's proficiency in transmitting and receiving acoustic waves. However, the inherent brittleness of ceramics can be a drawback.

In contrast, polymers such as Polyvinylidene Fluoride (PVDF) might not match the piezoelectric potency of ceramics but are favored for their adaptability, reduced acoustic resistance, and environmentally friendly nature since they are lead-free.

Combining the strengths of both ceramics and polymers, composite piezoelectrics emerge as versatile candidates. They harmonize the robust electromechanical coupling from ceramics with the adaptability and reduced acoustic impedance of polymers. Their compatibility with mediums like water or human tissue and their expansive bandwidth bolstered by a diminished mechanical quality factor render them suitable for a diverse range of uses.

3.2 Design of a single element transducer

In the field of ultrasound transducer modeling, attaining precise and dependable outcomes poses various significant challenges. This complexity arises from the need to successfully incorporate both piezoelectric and acoustic elements into a cohesive simulation model. As a step towards addressing these challenges, Krimholtz et al. (1970) introduced the KLM (Krimholtz, Leedom, and Matthaei) model [20], which employed an innovative approach by drawing an analogy to circuit network theory. In the KLM model, individual layers are portrayed as circuit components, but the model has limitations. Specifically, it fails to capture multidimensional effects, such as directivity and beam steering of acoustic waves. To accommodate these intricate aspects, more advanced modeling methodologies have been developed such as finite element models (FEM) incorporated in tools like COMSOL Multiphysics.

Utilizing COMSOL Multiphysics, it is possible to create a 2-D or 3-D multiphysics model that effectively simulates the behavior of the piezoelectric element as well as the transmission of acoustic pressure waves through solid media. While the KLM model provides a quick-to-run design tool, finite element methods, though more computationally intensive, deliver more accurate results that are closer to real-world physics. The present study intends first to design the matching layer stack and other parameters of the transducer via the KLM model and then optimize the entire transducer structure with the FEM model as illustrated in Figure 3.5. In particular, this chapter will delve deeper into the KLM and COMSOL simulations, elucidating their respective advantages, limitations, and potential for optimization.

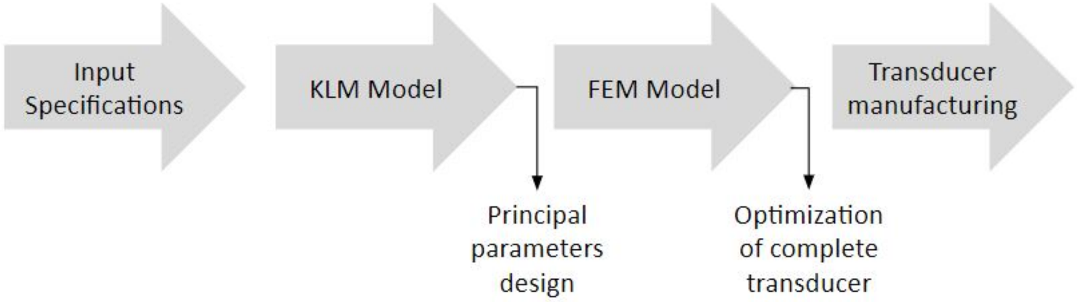

Figure 3.5: Visualization of the design steps

3.2.1 Electrical circuit model

The journey of modeling acoustic-electric transducers has traversed various theoretical constructs, beginning with the Mason model and culminating, for many researchers, with the KLM model. Each successive model incorporates an enhanced understanding of the intricacies involved in piezoelectric and acoustic transduction. Mason's model, shown in Figure 3.6 on top of the KLM model, was developed in the mid-20th century and it was a pioneering approach in the modeling of piezoelectric transducers. However, its scope was limited due to its low-frequency approximation and simplifying assumptions. The model didn't account for transmission and reflection at the boundaries between different materials and was thus only suitable for relatively simple, single-layer transducers. This triggered the need for a more comprehensive modeling framework.

Subsequent models aimed to overcome the limitations inherent in Mason's model. They incorporated multiple layers and accounted for different physical properties of the materials used. However, they often involved a trade-off between accuracy and computational complexity.

The KLM model (Figure 3.6), proposed in 1970, significantly improved upon the previous models. The KLM model has been particularly useful in the domain of ultrasound transducers because it offers a flexible, fast, and reasonably accurate tool for predicting transducer performance by drawing an analogy to circuit network theory.

One of the primary reasons why the KLM model is frequently used in ultrasound transducer modeling is its ability to consider the effect of multiple layers of different materials, with each layer having unique physical and acoustic properties. This feature is crucial because ultrasound transducers often contain multiple matching layers. The KLM model can accurately model the acoustic and electrical impedance of the different layers in the single-element transducer, as well as the reflections and transmissions at the interfaces between the layers.

Moreover, the KLM model's speed and computational efficiency make it an excellent tool for designing and optimizing transducers. It provides a balance between computational simplicity and the need for accurate performance prediction, which is essential in iterative design processes.

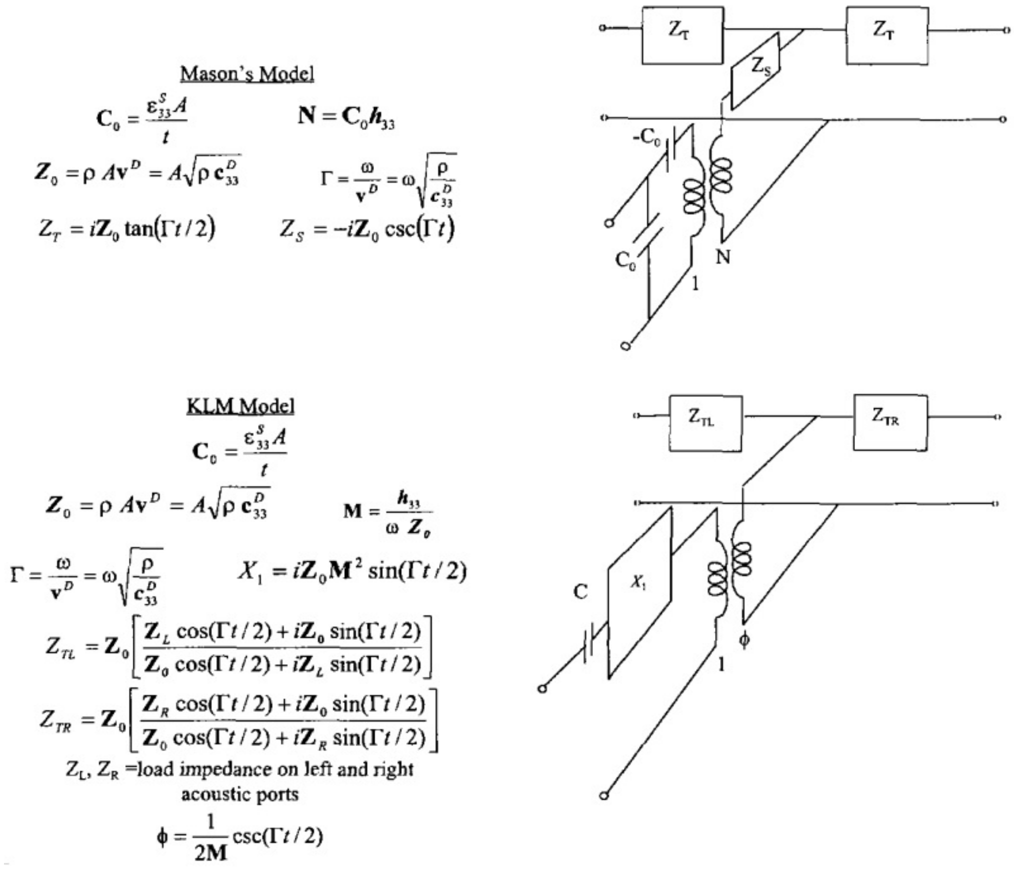

Figure 3.6: Mason and KLM model. Image by [21]

KLM Model

The operational understanding of a piezoelectric transducer can be enhanced with the use of a transmission line model such as the KLM model. This model allows the analysis of the transducer's electrical and mechanical properties and their interconnected behavior.

The KLM model for the piezoelectric crystal that characterizes the piezoelectric transducer is provided in Figure 3.7

In this model, V_3 and I_3 represent the applied voltage and current to the piezoelectric crystal. These inputs give rise to acoustic forces (F) and particle velocities (U) at the corresponding crystal surfaces. The internal particle velocities within the crystal are identified by subscripts F and B. Here, F designates forward-traveling waves heading toward interface 2, while the B subscript signifies backward-traveling waves directed toward interface 1. The notations + and - are used to distinguish waves in the right and left halves of the crystal, respectively. The acoustic impedances Z_1 and Z_2 pertain to the medium through which the crystal emits signals, namely the backing

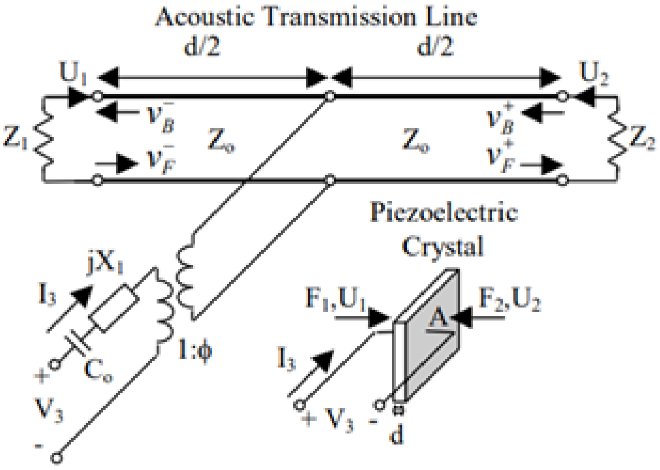

Figure 3.7: KLM model of a piezoelectric crystal.Image by [22]

layer and the body, respectively.

To complete the model, a capacitor (Co), an impedance (jX_1), and a transformer with the ratio (1:ϕ) are included, converting the electrical signal into the appropriate acoustical values.

The values for these parameters can be computed using the following formulas provided by Krimholtz et al.:

$$Z_0 = \rho c A \tag{3.2}$$

$$C_0 = \frac{{\epsilon_{33}}^S A}{d} \tag{3.3}$$

$$X_1 = \frac{{h_{33}}^2}{\omega^2 Z_0} \sin(\frac{\omega \cdot d}{c}) \tag{3.4}$$

$$\phi = \frac{\omega Z_0}{2h_{33}} \csc(\frac{\omega \cdot d}{2c}) \tag{3.5}$$

The model incorporates parameters such as the crystal's thickness (d) and area (A), along with the characteristic impedance (Zo) of the acoustic transmission line, which serves as a representation of the piezoelectric crystal.

In this context, ϵ_{33} represents the permittivity of the piezoelectric material when no voltage is applied, h_{33} stands for the piezoelectric pressure constant specific to the crystal, ρ denotes the density, and c signifies the speed of longitudinal sound waves within the crystal.

With the model parameters defined, the input impedance seen looking into port 3 is given by:

$$Z_{inKLM} = \frac{1}{J\omega C_0} + jX_1 + \frac{Z_a}{\phi^2} \tag{3.6}$$

Here, Z_a refers to the impedance observed when examining the acoustic transmission line. This impedance is derived from considering the impedances observed looking at interface 2 and interface 1, as indicated by Equation 3.7.

$$Z_a = \frac{Z_{L1} Z_{L2}}{Z_{L1} + Z_{L2}} \tag{3.7}$$

Specifically, the input impedances of the transmission lines leading to the two distinct interfaces are acquired through the application of the transmission line's input impedance formula:

$$Z_{L1,2} = Z_0 \frac{Z_{1,2} + jZ_0 \tan(\frac{\omega \dot{d}}{2c})}{Z_0 + jZ_{1,2} \tan(\frac{\omega \dot{d}}{2c})} \tag{3.8}$$

where $Z_{1,2}$ represents the characteristic acoustic impedance of the TL.

Impedance matching

Impedance matching forms a critical part of the design and operation of a piezoelectric transducer. When signals are transmitted from one part of a system to another, mismatches in impedance can result in signal reflections, leading to loss of power and distortion of the signal. In the context of a piezoelectric transducer, if the acoustic impedance of the transducer doesn't match the acoustic impedance of the medium into which it is radiating, this will lead to a significant amount of the ultrasound being reflected back into the transducer, rather than being transmitted into the tissue. Impedance matching aims to make the load impedance equal to the source impedance to maximize power transfer and minimize signal reflection.

Quarter wave impedance matching

A common technique used to achieve impedance matching in piezoelectric transducers is the use of quarter-wave layers. This method involves placing a layer of material, with a thickness equal to a quarter of the wavelength of the ultrasound wave (Figure 3.8), between the transducer and the medium. This layer is the so-called matching layer.

The quarter wave layer functions as a transformer, gradually transitioning the impedance from that of the piezoelectric crystal to that of the tissue. This process reduces the abrupt change in impedance, which leads to significant reflection

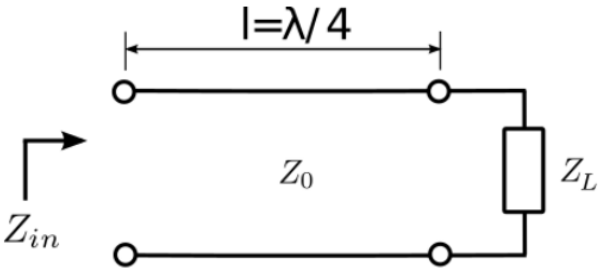

Figure 3.8: Quarter-wave impedance transformer. Image by [23]

at the interface of the transducer and the medium. The impedance of the quarter-wave layer is chosen as the impedance that allows to have an input impedance of the TL the most similar to the one of the piezoelectric material. The equation used to calculate the characteristic impedance Z_0 of the quarter-wave layer is given by:

$$Z_{in}(l) = Z_0 \frac{Z_L + Z_0 \tanh(\gamma l)}{Z_0 + Z_L \tanh(\gamma l)} \tag{3.9}$$

Where Z_{in} is (ideally) the impedance of the piezoelectric material, Z_0 is the characteristic impedance of the matching layer, and γ is the propagation constant given by the following formula.

$$\gamma = \alpha + i\beta \tag{3.10}$$

where α denotes the attenuation constant and β represents the phase constant, as defined by

$$\beta = \frac{2\pi}{\lambda} \tag{3.11}$$

This technique significantly improves the efficiency of power transfer and enhances the performance of the transducer in ultrasound imaging applications. It is especially useful in medical ultrasound devices, where it contributes to clearer images by increasing the proportion of the signal that is transmitted into the body, reducing reflections and hence improving the signal-to-noise ratio.

Design via KLM model

The optimization process of the transducer was so driven by a combination of the KLM model and quarter-wave impedance matching technique. The entire process was conducted in MATLAB, providing the flexibility to modify and adapt the model as needed.

The KLM model, allowed us to model the transducer as a two-port network. This made it possible to calculate the electrical input impedance and the power output for the transducer, an essential aspect in understanding its performance.

Impedance matching To achieve the highest efficiency, impedance matching was crucial as the impedance of piezoelectric materials and biological tissue differ significantly ($\sim 30 MRayls$). To determine the optimal impedance for the quarter-wavelength matching layer(s), we developed a MATLAB script. Initially, we considered a lossy transmission line to compute the matching layer characteristic impedances. However, due to high computational costs, we opted for a lossless transmission line. Subsequently, the suitability of the selected materials for the matching layer was validated using the KLM model.
For lossless TL, there are two distinct methods used to identify the ideal acoustic impedance of the quarter-wavelength matching layer which yield different outcomes, thus both of them have been evaluated.
The first method focuses on optimizing energy transfer across the two interfaces at play considering the piezoelectric element as infinite. The acoustic impedance of the matching layer, in this case, is represented by:

$$Z_m = \sqrt{Z_a Z_p} \tag{3.12}$$

This can be extended for a scenario involving n matching layers, where the characteristic acoustic impedance of the jth matching layer is described as:

$$Z_{mj} = \sqrt[n+1]{{Z_a}^j {Z_p}^{n-j+1}} \tag{3.13}$$

The second approach, credited to Desilets et al. [24], takes into account the finite thickness of the piezoelectric element. In this case, maximum efficiency and optimum bandwidth are imposed in order to determine the acoustic impedance of the matching layer and the number of layers required. Specifically, a single matching layer's acoustic impedance is:

$$Z_m = {Z_a}^{\frac{2}{3}} * {Z_p}^{\frac{1}{3}} \tag{3.14}$$

And for two layers:

$$Z_{m1} = {Z_a}^{\frac{3}{7}} * {Z_p}^{\frac{4}{7}} \tag{3.15}$$

$$Z_{m2} = {Z_a}^{\frac{6}{7}} * {Z_p}^{\frac{1}{7}} \tag{3.16}$$

It's evident that the two methods differ, with the Desilets approach often resulting in lower acoustic impedance values for the matching layers. Nevertheless, both methods agree on the need for materials with low acoustic impedance, and given that acoustic impedance is defined by Z = ρc, this implies the necessity for materials with reduced density (ρ) and acoustic velocity (c) when choosing matching layer materials. Typically, these low-density materials are porous, and their acoustic attenuation coefficient is naturally high, increasing with frequency. A low acoustic velocity results in extremely thin ($\lambda/4$) matching layers, especially at elevated frequencies for this reason manufacturing techniques should be carefully investigated.

Impedance matching results The impedance-matching Matlab script was designed to compute the values for one and two matching layers, offering a broad perspective of the variations and possibilities. The calculations considered the acoustic impedance of the piezoelectric material, the body, and the backing layer acoustic impedance as the loads. Furthermore, the choice of the ultrasound transducer's central frequency was carefully considered. A frequency of 6.6 MHz was selected specifically to image the gastrocnemius muscle, a superficial muscle located in the calf. This frequency was deemed optimal for capturing high-resolution images of this muscle since ultrasound transducers with a central frequency between 5-10MHz are optimal for imaging superficial muscles, while frequencies between 1-5MHz are better suited for imaging deeper muscles. For the piezocrystal, PZT-5A was selected. This choice was driven by two primary reasons: PZT is a prevalent material for ultrasound transducers due to its consistent performance, and the 5A variant specifically offers stable properties across varying temperatures. When considering the backing layer, several materials have been identified, such as a combination of Tungsten powder, microbubbles, and Epotek 301, as detailed in [25]. However, the KLM Model just requires to indicate the characteristic acoustic impedance of the backing layer and it has been found that, typically, the impedance of the backing layer hovers around 6.5 MRayls. This impedance value was, therefore, adopted in our simulation studies.

# Matching Layers	First Approach [MRayls]	Second Approach [MRayls]
One Matching Layer	6.73	4.08
Two Matching Layer	11.09 - 4.08	8.3 - 2.30

Table 3.1: Ideal matching layers acoustic impedance

With the ideal impedance values in hand (Table 3.1), a search for suitable matching layer materials was undertaken. The aim was to find materials with acoustic impedance as close as possible to the calculated ideal values, thus ensuring maximum power transfer and minimizing reflection at the material interfaces. In order to find the right material, the table in Figure 3.9 was used.

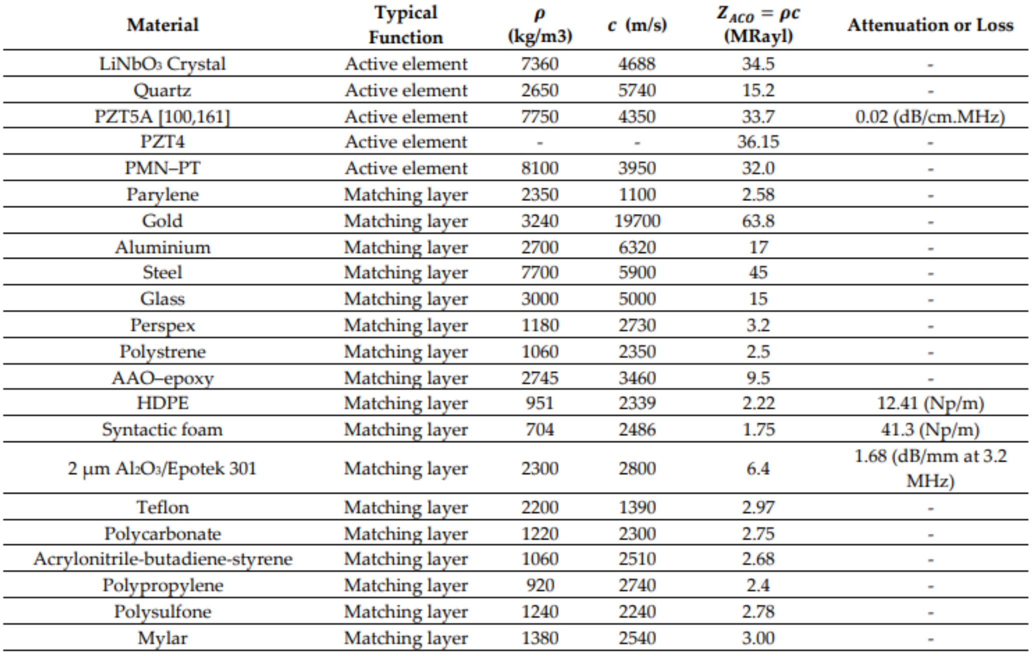

Material	Typical Function	ρ (kg/m3)	c (m/s)	$Z_{ACO} = \rho c$ (MRayl)	Attenuation or Loss
$LiNbO_3$ Crystal	Active element	7360	4688	34.5	-
Quartz	Active element	2650	5740	15.2	-
PZT5A [100,161]	Active element	7750	4350	33.7	0.02 (dB/cm.MHz)
PZT4	Active element	-	-	36.15	-
PMN–PT	Active element	8100	3950	32.0	-
Parylene	Matching layer	2350	1100	2.58	-
Gold	Matching layer	3240	19700	63.8	-
Aluminium	Matching layer	2700	6320	17	-
Steel	Matching layer	7700	5900	45	-
Glass	Matching layer	3000	5000	15	-
Perspex	Matching layer	1180	2730	3.2	-
Polystrene	Matching layer	1060	2350	2.5	-
AAO–epoxy	Matching layer	2745	3460	9.5	-
HDPE	Matching layer	951	2339	2.22	12.41 (Np/m)
Syntactic foam	Matching layer	704	2486	1.75	41.3 (Np/m)
2 µm Al_2O_3/Epotek 301	Matching layer	2300	2800	6.4	1.68 (dB/mm at 3.2 MHz)
Teflon	Matching layer	2200	1390	2.97	-
Polycarbonate	Matching layer	1220	2300	2.75	-
Acrylonitrile-butadiene-styrene	Matching layer	1060	2510	2.68	-
Polypropylene	Matching layer	920	2740	2.4	-
Polysulfone	Matching layer	1240	2240	2.78	-
Mylar	Matching layer	1380	2540	3.00	-

Figure 3.9: Acoustic properties of typical piezoelectric transducer materials and media. Table by [26]

Building on our findings, a comprehensive breakdown of the matching layers employed in two distinct configurations is presented. Table 3.2 shows the materials for configurations employing a singular matching layer, whereas Table 3.3 delineates configurations with a dual-layer approach.

First Matching Layer	Impedance [MRayls]
2 $\mu m Al_2O_3$/ Epotek 301	6.4
AAO-Epoxy	9.5
Epotek 301	2.8
HDPE	2.22

Table 3.2: List of the materials and relative acoustic impedance for ultrasound piezoelectric transducer with one matching layer

First Matching Layer	Impedance FML [MRayls]	Second Matching Layer	Impedance SML [MRayls]
Aluminum	17	HDPE	2.22
Aluminum	17	Epotek 301	2.8
AAO-Epoxy	9.5	Epotek 301	2.8
2 $\mu m Al_2O_3$ / Epotek 301	6.4	Aluminum	17
2 $\mu m Al_2O_3$ / Epotek 301	6.4	HDPE	2.22

Table 3.3: List of the materials and relative acoustic impedance for ultrasound piezoelectric transducer with two matching layer

Following the identification of suitable materials for the matching layer, they were seamlessly integrated into the KLM model. All the specific material properties utilized in the KLM model are comprehensively outlined in Table 3.4.

Material	Speed of sound [m/s]	Density [$\frac{kg}{m^3}$]	Attenuation [Np/m]
PZT-5A	3895.5	7750	0.2 × MHz
AAO-Epoxy	3460	2745	2.88
Epotek 301	2640	1048	119.73
HDPE	2339	951	12.43
Aluminum	6320	2700	0.46
2 $\mu m Al_2O_3$ / Epotek 301	2800	2300	193.4

Table 3.4: Properties of the materials used in the KLM model

Results

In this section, we delve into the comprehensive outcomes derived from the KLM model simulations. Recognizing the intricacies involved in the matching process, we've structured our results to specifically cater to two distinct scenarios: the utilization of a single matching layer and that of two matching layers.

One matching layer

In the quest for optimal transducer efficiency, the selection of matching layers stands paramount. Figure 3.10 underscores this point by presenting the efficiency metrics for transducers employing a singular matching layer. Specifically, this figure highlights two distinct configurations: AAO-epoxy and 2 $\mu m Al_2 O_3$ / Epotek 301, which are characterized by acoustic impedances of 9.5 MRayls and 6.4 MRayls, respectively.

As we've established earlier, for optimal impedance matching, the acoustic impedance of the matching layer ideally aligns around 6.73 MRayls or 4.08 MRayls. Consequently, the choices we've illustrated in Figure 3.10 are closely aligned with these ideal metrics.

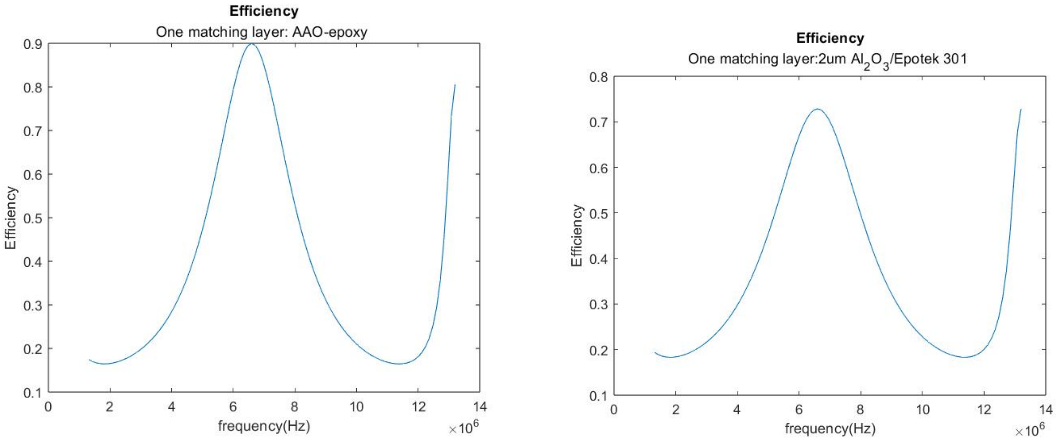

Figure 3.10: Ultrasound piezoelectric transducer with one matching layer : AAO-epoxy on the left and 2 $\mu m Al_2 O_3$ / Epotek 301 on the right

In contrast, Figure 3.11 delineates configurations where matching layers with an impedance of approximately 2 MRayls are utilized. Given the disparity from our ideal impedance values, it's unsurprising that these configurations exhibit diminished efficiency. This stark comparison underlines the critical role of matching layers in influencing transducer performance and emphasizes the necessity for meticulous layer selection.

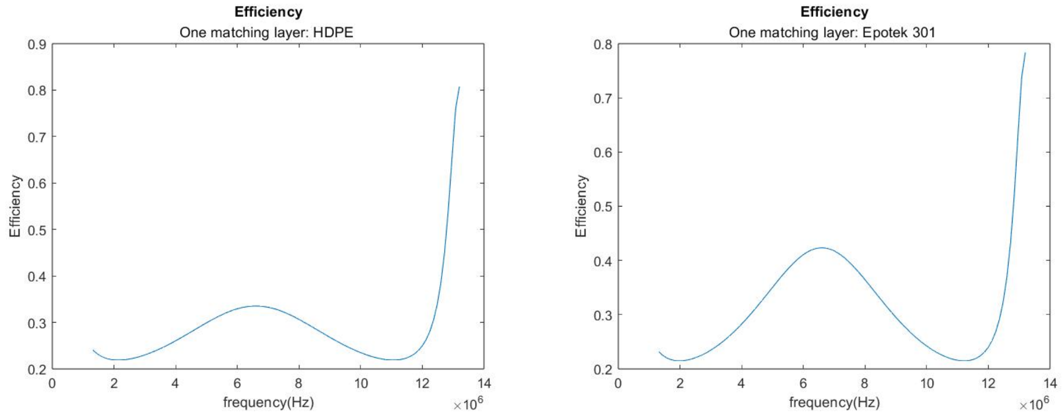

Figure 3.11: Ultrasound piezoelectric transducer with one matching layer: HDPE on the left and Epotek 301 on the right

Two matching layers Transitioning from single to double matching layers offers intriguing possibilities for enhancing the efficiency of transducers. In the succeeding set of simulations, our focus pivots towards these dual-layer configurations. Based on theoretical calculations, the optimal impedance values for dual-layered structures were identified to be 11-4 MRayls or 8-2.3 MRayls. With this in mind, we pursued a few promising combinations to not only align with these ideal impedances but to also understand the interplay between the two characteristic acoustic impedances. The following combinations were earmarked for simulations:

- Aluminum [17 MRayls]- HDPE [2.22 MRayls]
- Aluminum [17 MRayls] - Epotek 301 [2.8 MRayls]
- Aluminum [17 MRayls] - 2um AL2O3/Epotek 301 [6.4 MRayls]
- AAO epoxy [9.5 MRayls] - Epotek 301 [2.8 MRayls]
- 2um AL2O3/Epotek 301 [6.4 MRayls] - HDPE [2.22 MRayls]

A comparative analysis revealed interesting findings. As showcased in Figure 3.12, certain combinations like AAO epoxy - Epotek 301, Aluminum - HDPE, and Aluminum - Epotek 301 exhibited commendable efficiencies. Conversely, Figure 3.13 highlights the relative underperformance of the other combinations, particularly at the center frequency (6.6MHz). This analysis underscores the significance of aligning the acoustic impedances closely with the ideal values and in case of less optimal scenarios, it is preferable to have a first layer with a higher impedance and a second layer with a lower impedance.

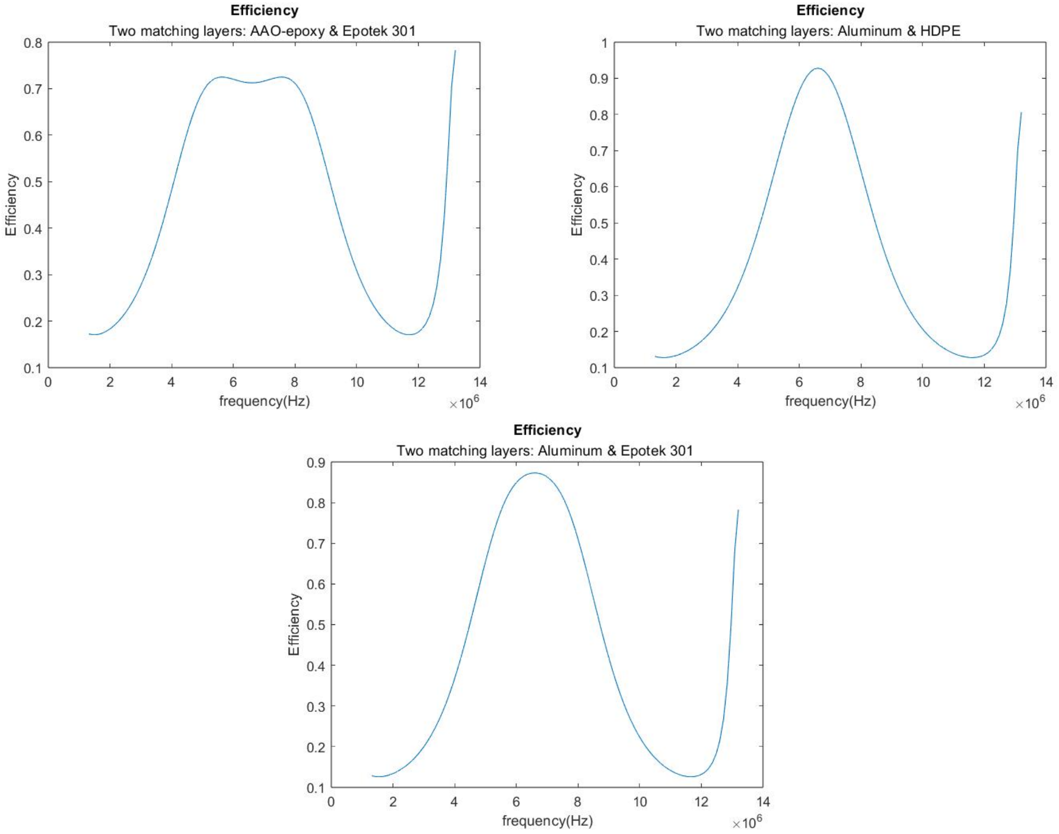

Figure 3.12: Ultrasound piezoelectric transducer with two matching layers

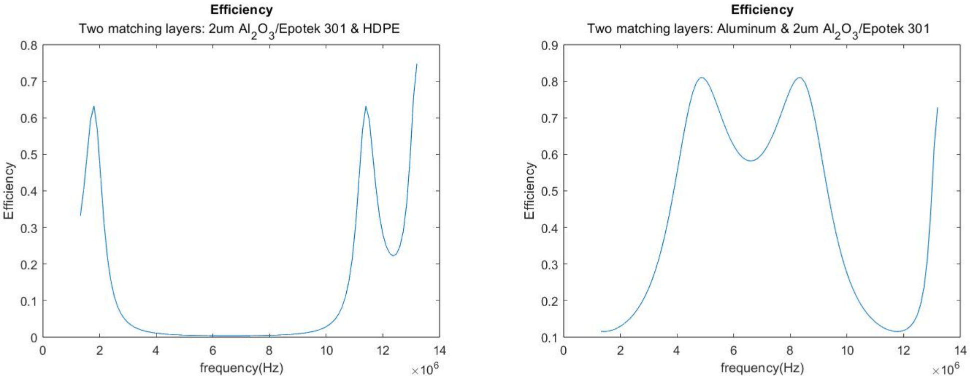

Figure 3.13: Ultrasound piezoelectric transducer with two matching layers

One overarching observation that emanates from this analysis is also the enhancement of bandwidth when transitioning to dual matching layers. In essence, increasing the number of matching layers serves as an effective strategy to bolster the transducer's bandwidth. Another avenue to augment bandwidth could also be employing matching layers of non-uniform materials with a continuous decline in acoustic impedance along the ultrasonic propagation direction [27].

3.2.2 Finite element model

Having explored the theoretical underpinnings of piezoelectric transducers using the KLM model, our attention now turns towards a more advanced approach using finite element modeling. This shift allows us to delve deeper into the complexities of transducer performance and, as a consequence, be able to optimize the design.
The use of finite element models, particularly through COMSOL Multiphysics, provides a versatile and robust platform for analyzing transducer performance. COMSOL, a widely utilized finite element analysis software, excels at simulating intricate multiphysics behavior, providing a comprehensive and detailed understanding of the transducer's operational characteristics.
Despite their immense utility, finite element models require significantly more computational power compared to their mathematical counterparts like the KLM model. However, the wealth of detail and insight they provide justifies their usage in analyzing complex systems.
In the upcoming section, the powerful capabilities of COMSOL Multiphysics will be leveraged to simulate and optimize the piezoelectric transducer design, enriching the understanding and comparison framework established with the KLM model.

Modeling

The developed model is a 2-D axisymmetric representation exploiting the axial symmetry of the system to reduce the computational cost. It employs the integrated Acoustic-Piezoelectric Interaction, Frequency Domain multi-physics interface. This interface encapsulates three primary physics interfaces: Pressure Acoustics, Solid Mechanics, and Electrostatics. Pressure Acoustics addresses the wave equation in the media around the transducer, whereas the other two interfaces are dedicated to modeling the piezoelectric effect and solid structures.

Setup

The configuration of the model aligns with a conventional ultrasound piezoelectric transducer setup [28]. To enhance its representation of real-world scenarios, two electrodes and the backing layer material have been incorporated.
Rooted in fundamental physics and insights from previous simulations, we've established the model's geometric parameters. A crucial aspect in the design of ultrasound transducers is achieving resonance for efficient energy conversion. For a piezoelectric transducer to resonate optimally at a frequency f_0, the thickness of the piezoelectric element T_{pzt} should be half the wavelength ($\frac{\lambda_0}{2}$). This is expressed as:

$$T_{pzt} = \frac{\lambda}{2} \tag{3.17}$$

When the thickness is $\frac{\lambda}{2}$ the piezoelectric element vibrates most efficiently, leading to the maximum transfer of electrical energy to acoustic energy. Suppose we are aiming to maximize the transmission coefficient around 6.6MHz, the wavelength at this frequency is equal to the following:

$$\lambda = \frac{c_{PZT}}{f_0} = 0.59mm \tag{3.18}$$

This necessitates a piezoelectric thickness of 0.295 mm, which is half of the identified wavelength. For the matching layers, the objective is to ensure impedance continuity between the piezoelectric material and the human body, minimizing reflections at the interface. This requires the matching layer's thickness T_{Layer} to be a quarter of the wavelength $\frac{\lambda}{4}$

$$T_{Layer} = \frac{\lambda}{4} \tag{3.19}$$

While this quarter-wavelength thickness offers the optimal transmission coefficient for our chosen matching material, it may not cater to potential bandwidth requirements. Nonetheless, it provides an excellent baseline from which to adjust and optimize material thickness dimensions.

Materials and Geometry

The acoustic piezoelectric transducer components feature PZT-5A as the chosen piezoelectric material. This choice of PZT-5A, as previously mentioned, is grounded in existing literature and is commonly used in acoustic transmission systems. The pertinent material properties, such as density, speed of sound, acoustic impedance, and all the other properties that were necessary during the KLM simulations and the COMSOL modeling, are detailed in Table 3.5.

Specifically, the equations employed to calculate h_{33} based on the table's properties are given by Equations 3.20, and 3.21.

$${c_{33}}^E = {c_{33}}^D(1 - {k_t}^2) \tag{3.20}$$

$$h_{33} = k_t\sqrt{\frac{{c_{33}}^D}{{\epsilon_{33}}^S}} \tag{3.21}$$

Property	**PZT-5A**
c	3895.5 m/s [29]
ρ	7750 kg/m^3 [29]
k_t	0.49 [30]
Q_m	75 [31]
$tan\delta$	<0.02 @ 1kHz [32]
k_{33}	0.72 [30]
${\epsilon_{33}}^S{\epsilon_0}^{-1}$	826.6 [29]
${c_{33}}^E$	1.109 Pa × 10^{11} [29]
h_{33}	2.19 $\frac{V}{c^2}$ × 10^9 [Eq. 3.21]

Table 3.5: PZT-5A properties

In the beginning, the leg and the backing layer representations consisted of an acoustic domain symbolizing them, as depicted in Figure 3.14 in pink and in black respectively. However, to optimize computational efficiency, they were later transformed into an acoustic impedance load, achieving comparable results.

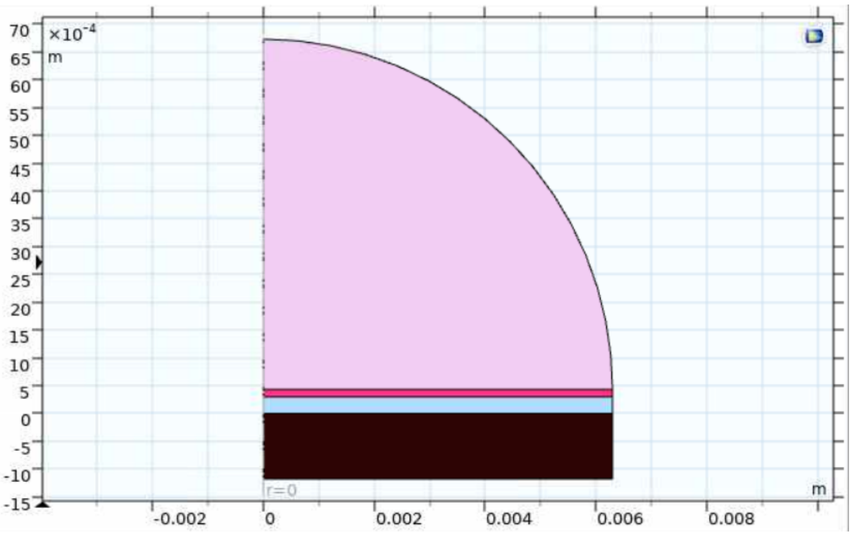

Figure 3.14: Model of the system (from bottom to top: backing layer, piezoelectric layer, matching layer, body)

As previously mentioned, the materials and dimensions of the matching layer(s) were derived from the KLM model, primarily using the quarter-wavelength method as a foundation.

Boundary condition

The boundary conditions of the piezo-acoustic transducer model are meticulously defined to mirror the device's real-world operational environment and its intrinsic physics.

These conditions emulate the conversion of an electrical signal into a pressure wave by a piezoelectric element as it traverses multiple material layers. Within the model, the piezoelectric layer is endowed with physical attributes sourced from two distinct simulation modules: Electrostatics and Solid Mechanics. Upon subjecting this layer to a voltage, specifically a unit voltage in this study, a pressure wave propagates through the acoustic channel. The terminus of the transmission material is characterized by an acoustic impedance boundary condition, reflecting the presumed adjacency of the human body. Additionally, to simulate the backing layer and streamline computational demands, an acoustic impedance boundary condition is applied to the lower electrode.

Piezoelectric losses

Given the intrinsic nature of piezoelectric materials, which simultaneously incorporate both mechanical and electrical phenomena, it's essential to understand that their modeling accounts for multiple types of losses. These include mechanical, electrical, and electromechanical coupling losses, as illustrated in Figure 3.15.

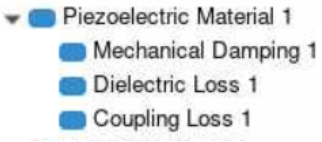

Figure 3.15: Piezoelectric material type of losses

When considering mechanical damping, it's necessary to define a structural loss factor. Specifically, this factor is given by:

$$\gamma_s = \frac{2\alpha\beta}{\alpha^2 + \beta^2} \tag{3.22}$$

In this equation, α represents the attenuation constant and β the phase constant. Regarding the dielectric loss, the factor $tan\delta$ must be specified, which is inherent to the piezoelectric material's properties. As for the coupling losses, they are predefined in the material data sourced from the COMSOL material library and merely need to be activated for the simulation.

Meshing

For this study, a free triangular mesh was utilized throughout the entire transducer. The selection of the mesh size was informed by the findings from previous finite element studies [33]. In these studies, it was demonstrated that the optimal element size should be correlated to the wavelength of the wave. More explicitly, one can derive the element size by multiplying the equation for the wavelength by a factor of $\frac{1}{n}$, yielding:

$$size = \frac{c_{min}}{f_{max} \times n} \tag{3.23}$$

Here, the element size corresponds to a desired count of 'n' elements within a wavelength. Wilt's research found that for n λ values ranging between 5 and 10, the model started converging toward an accurate solution. However, it didn't achieve an error margin of less than 1.0% across all frequencies until n reached 12. For this reason, to strike a balance between accuracy and computational efficiency, a value of n=12 was chosen for the meshing. In Figure 3.16 is possible to see the final mesh utilized.

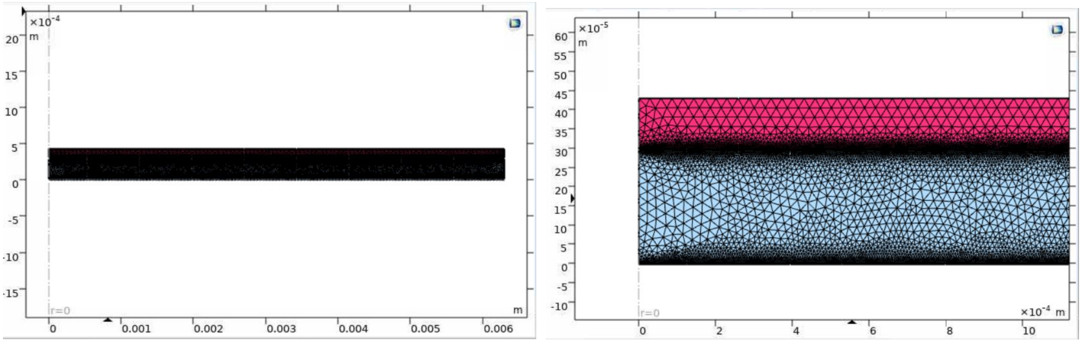

Figure 3.16: Mesh utilized to simulate the transducer

Results

In the subsequent section, we present the outcomes obtained from the COMSOL simulations, shedding light on the implications and performance of our piezoelectric transducer model. Our findings are organized akin to our earlier KLM model results, addressing two specific scenarios: employing a single matching layer versus the use of dual matching layers. The choice between these configurations holds significant weight in determining transducer efficiency. For consistency, we've mirrored the matching layers used in the KLM model in our COMSOL simulations, but will only be detailing the most pertinent results here.

One matching layer The efficiency metrics for transducers equipped with a lone matching layer are visually represented in Figure 3.17 and Figure 3.18. On the left, it is possible to find the COMSOL simulation results, while the corresponding KLM results are displayed on the right.
Delving deeper, Figure 3.17 provides a comparative insight between the efficiencies derived from the COMSOL and KLM models for a transducer utilizing AAO epoxy as its matching layer. In contrast, Figure 3.18 delineates results for the transducer featuring the $2\mu m Al_2O_3$/Epotek 301 composite as the matching layer.

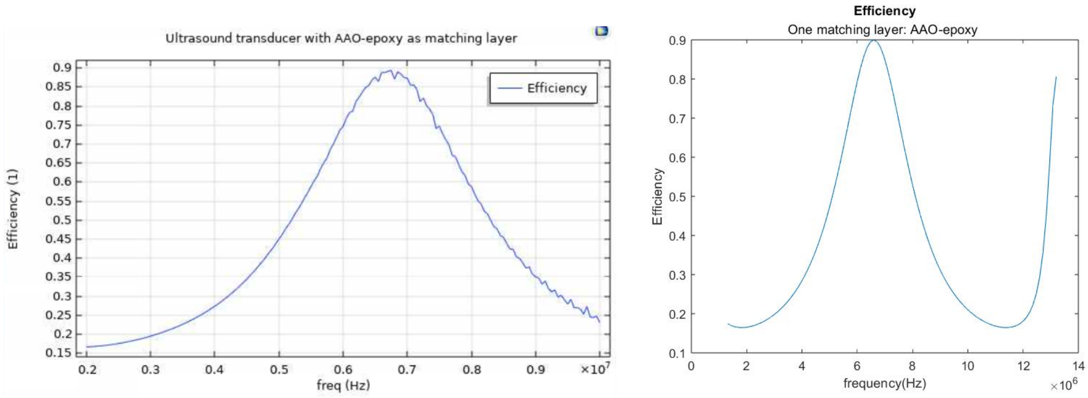

Figure 3.17: COMSOL transducer simulation with AAO-epoxy as matching layer on the left and on the right KLM model simulation

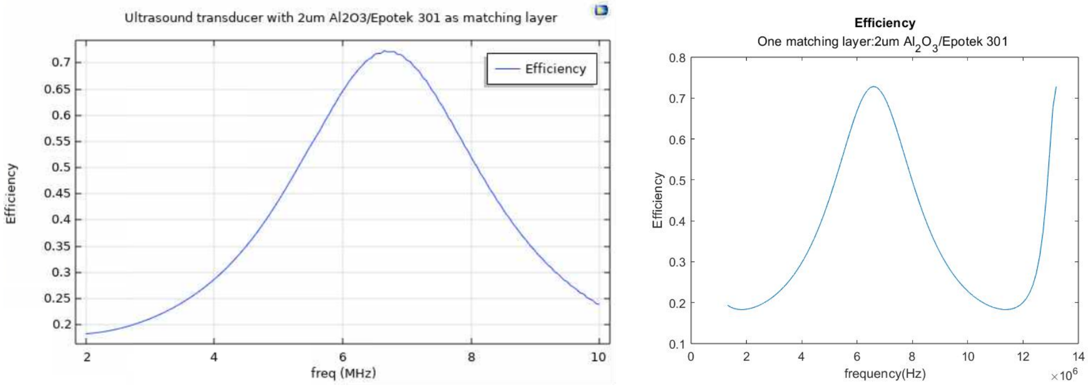

Figure 3.18: COMSOL transducer simulation with 2 $\mu m Al_2O_3/Epotek301$ as matching layer on the left and on the right KLM model simulation

In both instances, the discrepancy in efficiency magnitude is negligible, whereas the differences in bandwidth and waveform are almost absent.

Two matching layers Sequentially, Figure 3.20 presents a comparative analysis between the COMSOL simulation results and the KLM model outcomes, emphasizing transducers designed with two matching layers.

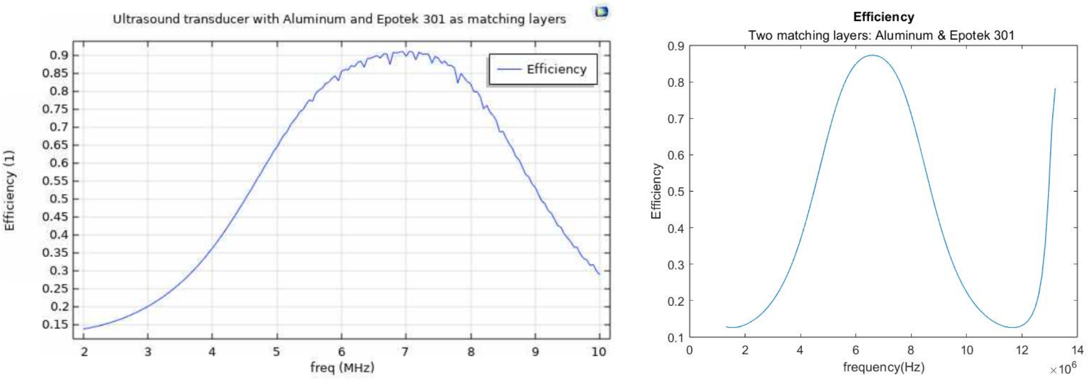

Figure 3.19: COMSOL transducers simulation with two matching layers on the left and on the right the respective KLM model simulation

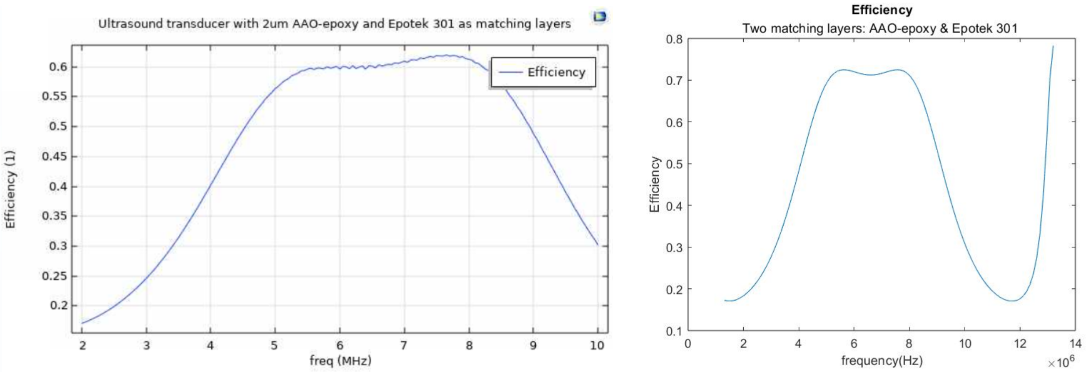

Figure 3.20: COMSOL transducers simulation with two matching layers on the left and on the right the respective KLM model simulation

The FEM simulation results further reinforce our earlier observations. As the number of matching layers increases, the bandwidth expands, notably when utilizing the AAO epoxy and Epotek 301 combination. This combination is indeed favored in ultrasonic transducer applications due to its broad bandwidth [25].

3.2.3 KLM vs FEM

Upon examination of both one-matching layer structures and two-layer ones, all transducer configurations exhibit a small discrepancy between the finite element model (COMSOL) and KLM model outcomes, specifically in the magnitude of the transmission coefficient. Despite this discrepancy, the waveforms and bandwidth of the responses are remarkably similar across both models. Such differentiation might stem from COMSOL's methodology in calculating the speed of sound, which pivots on the elastic properties of materials and can be swayed by elements like mesh granularity. Another potential source of the observed discrepancies might be the more comprehensive accounting of losses within the COMSOL model, leading to variations solely in the magnitude of the transmission coefficient. Nonetheless, the waveform remains a paramount design consideration, as the ultimate objective revolves around achieving a robust transmission coefficient spanning a specified bandwidth.

3.2.4 Conclusions

At this stage, with both the KLM and COMSOL models developed and verified to produce similar outcomes, it becomes feasible to proceed with the design of the complete ultrasound transducer system. The close agreement between the two models enhances confidence in the predictive capabilities of each, assuring that they can be reliably used for the optimization and development of transducer configurations.

In particular, the COMSOL finite element model offers the advantage of studying the transducer behavior in finer detail. For instance, it provides the capability to simulate spatial variations of stress and strain, complex geometries, and allows for a more comprehensive treatment of boundary conditions. This in-depth analysis can be invaluable for designing transducers that are not just idealized versions but practical, real-world devices. This may include adjustments based on temperature dependencies, anisotropic materials, or even non-linear effects which are difficult to account for in simpler models like KLM.

Moreover, the finite element model enables us to scrutinize how minor alterations in material properties or layer dimensions can influence the overall performance, helping to fine-tune the design parameters for optimal results. It also allows for the simulation of multi-layer structures with different combinations of materials, thereby providing a wider landscape for design optimization.

In summary, the development and cross-verification of the KLM and COMSOL models pave the way for the full-scale design of ultrasound transducers. While the KLM model serves as a quick and insightful tool for initial design considerations, the COMSOL model serves as a robust tool for a more exhaustive and detailed analysis. The complementary nature of these two modeling approaches allows for a more holistic and reliable transducer design process, fulfilling both quick turn-around and detailed scrutiny requisites.

Chapter 4

Evaluation of muscle velocity

4.1 Introduction

The importance of accurate and efficient measurement of the velocity of muscle-tendon units (MTUs) cannot be overstated. With applications ranging from the control of wearable devices [5], to the understanding of age-related changes in musculoskeletal health [34], and even to the early detection and prevention of tendon injuries [35] [36], the study and quantification of muscle-tendon biomechanics have far-reaching implications. However, traditional methodologies, such as joint movement analysis and B-Mode imaging analysis, have been hampered by computational expense and time-consuming data processing procedures. Recent approaches utilize optical flow methods on B-mode imaging [5] for faster data processing but, despite their potential, they are not without their own set of limitations, including variable accuracy dependent on the tissue structure under examination.

In response to these challenges, we planned to propose a novel solution for measuring velocity in MTUs, a computationally simple ultrasound method based on spectral Doppler. Unlike its predecessors, this method is independent of tissue structure, allowing for accurate measurements irrespective of tissue characteristics that can significantly vary among individuals. Furthermore, the spectral Doppler method provides a more efficient computational process, thereby reducing the required processing time and resources.

However, due to constraints on time, we were unable to fully realize all aspects of our planned initiative. This chapter delves into the methodology we devised to showcase that utilizing Doppler techniques, as opposed to Optical Flow methods, can reduce computational overhead and enhance the precision of detected muscle velocities. Initially, we focus on designing a phantom to calibrate the measurement system. Following this, we present a comprehensive introduction to both the Optical Flow and Doppler methods, detailing their applications and operational procedures.

4.2 Literature review

As we delve further into the understanding of muscle velocity evaluation, it becomes essential to survey the landscape of existing research in this area. This chapter provides a comprehensive literature review, taking into account the various studies, methodologies, and findings that have contributed to our current understanding of muscle velocity evaluation. We will explore the range of techniques employed in past research and the outcomes that have shaped current practices and set the stage for future investigations. This review will help us to contextualize our study within the broader field, identify gaps in the existing knowledge, and provide a rationale for the current research.

4.2.1 Velocity and strain measuring methods

The velocity of muscle-tendon units (MTUs) can be measured through a variety of methods. Two common approaches include using joint movement and analysis of B-Mode imaging as previously stated. However, both come with their limitations, such as computational expense and time-consuming data processing. Thus, newer techniques have been developed to overcome these obstacles.

Joint Movement Analysis

One of the traditional ways to estimate the velocity and strain of MTUs involves analyzing the movement of the joint associated with the muscle-tendon unit under investigation. The joint angles are often measured using motion capture systems. This data is then used to calculate the velocity and strain of the muscle-tendon unit using mathematical models of the human body and its joints. However, this approach can be limited by a lack of direct measurement of muscle and tendon movement and it also requires complex and computationally intensive data processing, which can be time-consuming.

B-Mode Imaging Analysis

Another common approach is the analysis of B-Mode imaging. This method involves creating two-dimensional images based on the reflection of ultrasound waves, enabling the visualization of the interior structure of the muscle-tendon unit. Although B-Mode imaging provides detailed images, data processing is semi-automated and requires substantial computational resources indeed extracting meaningful data demands robust computational processes, often leaning on semi-automated techniques. Furthermore, the precision of the measurements can be influenced by the angle at which the ultrasound is directed and the skill level of the operator. As such, while B-Mode imaging provides a wealth of information, its full potential is harnessed best when managed with expertise and precision.

Optical Flow Methods

To overcome the limitations of the analysis of the joint kinematics and B-mode images, researchers have employed optical flow methods on B-Mode imaging. Optical flow analysis involves tracking the movement of speckle patterns within the ultrasound images. The change in the speckle pattern from frame to frame can be used to estimate the velocity of MTUs. This method provides faster processing times and can potentially provide more direct measurements of muscle-tendon movement. However, optical flow method results depend on the tissue structure being examined, and it still requires significant computational resources.

Spectral Doppler Method

In the quest for a more efficient and accurate technique, the spectral Doppler method has been proposed. This approach involves measuring the shift in frequency (Doppler effect) of the reflected ultrasound waves caused by the motion of the tissue, which provides a measure of velocity. Unlike the previously mentioned techniques, the spectral Doppler method is independent of tissue structure and offers a simpler and more efficient computational process. This leads to more accurate and quicker measurements of the velocity in MTUs.

4.2.2 Ground truth

Precise velocity measurements of muscles are crucial for gaining insights into their behavior and optimizing performance, however, obtaining accurate velocity data from real human muscles poses inherent challenges due to complexities and influencing factors. For this reason, this chapter unveils a solution: the development of a muscle-mimicking material to calibrate the measuring system. By creating an artificial muscle that mimics real muscles, we establish a controlled and standardized environment for obtaining accurate velocity measurements. This section goes through an in-depth exploration of the material's development, fabrication, and utilization in the benchtop test setup.

Muscle mimicking materials

Phantoms are indispensable in medical research, simulating tissue to assess clinical imaging, therapeutic devices, and medical procedures in a risk-free test environment, eliminating harm to animals or humans. Given the varied uses, there's a plethora of TMM designed to emulate the pertinent properties of biological tissue. The table in Figure 4.1, published by Conor K McGarry et al. (2020), provides a summary of the key acoustic and mechanical traits of various tissue types while Figure 4.2 reports the sound properties of TMMs often used for different ultrasound purposes. A few of these materials will be further analyzed later.

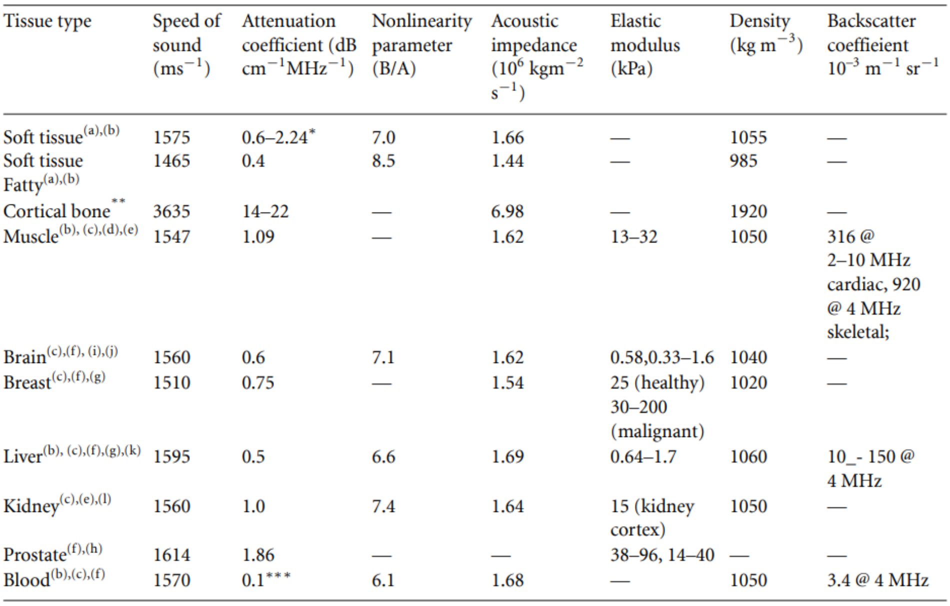

Tissue type	Speed of sound (ms^{-1})	Attenuation coefficient (dB cm^{-1}MHz^{-1})	Nonlinearity parameter (B/A)	Acoustic impedance (10^6 kgm^{-2} s^{-1})	Elastic modulus (kPa)	Density (kg m^{-3})	Backscatter coeffieient 10^{-3} m^{-1} sr^{-1}
Soft tissue$^{(a),(b)}$	1575	0.6–2.24*	7.0	1.66	—	1055	—
Soft tissue Fatty$^{(a),(b)}$	1465	0.4	8.5	1.44	—	985	—
Cortical bone**	3635	14–22	—	6.98	—	1920	—
Muscle$^{(b), (c),(d),(e)}$	1547	1.09	—	1.62	13–32	1050	316 @ 2–10 MHz cardiac, 920 @ 4 MHz skeletal;
Brain$^{(c),(f), (i),(j)}$	1560	0.6	7.1	1.62	0.58,0.33–1.6	1040	—
Breast$^{(c),(f),(g)}$	1510	0.75	—	1.54	25 (healthy) 30–200 (malignant)	1020	—
Liver$^{(b), (c),(f),(g),(k)}$	1595	0.5	6.6	1.69	0.64–1.7	1060	10_- 150 @ 4 MHz
Kidney$^{(c),(e),(l)}$	1560	1.0	7.4	1.64	15 (kidney cortex)	1050	—
Prostate$^{(f),(h)}$	1614	1.86	—	—	38–96, 14–40	—	—
Blood$^{(b),(c),(f)}$	1570	0.1***	6.1	1.68	—	1050	3.4 @ 4 MHz

Figure 4.1: Acoustic and mechanical characteristics of tissues. Table by [37]

Generally, TMMs mimic human tissue, serving to fine-tune imaging instruments, train healthcare professionals, and pioneer treatments. Specifically, materials designed to resemble muscles for ultrasound applications replicate the acoustic characteristics of muscle tissues. These can be crafted from a range of substances, from agar mixtures to synthetic materials like polyvinyl alcohol cryogels and gel wax, among others. Each offers distinct properties fitting different requirements. Subsequent sections will delve into the materials with the most promising properties to mimic a muscle, elaborating on their attributes.

Agar

Agar-based Tissue Mimicking Materials are commonly used. The material is characterized by a speed of sound of 1541-1547 $\frac{m}{s}$, density of 1054 $\frac{kg}{m^3}$ and attenuation coefficient of 0.5 $\frac{dB}{cmMHz}$ whose dependency from the frequency becomes non-linear above 20MHz.

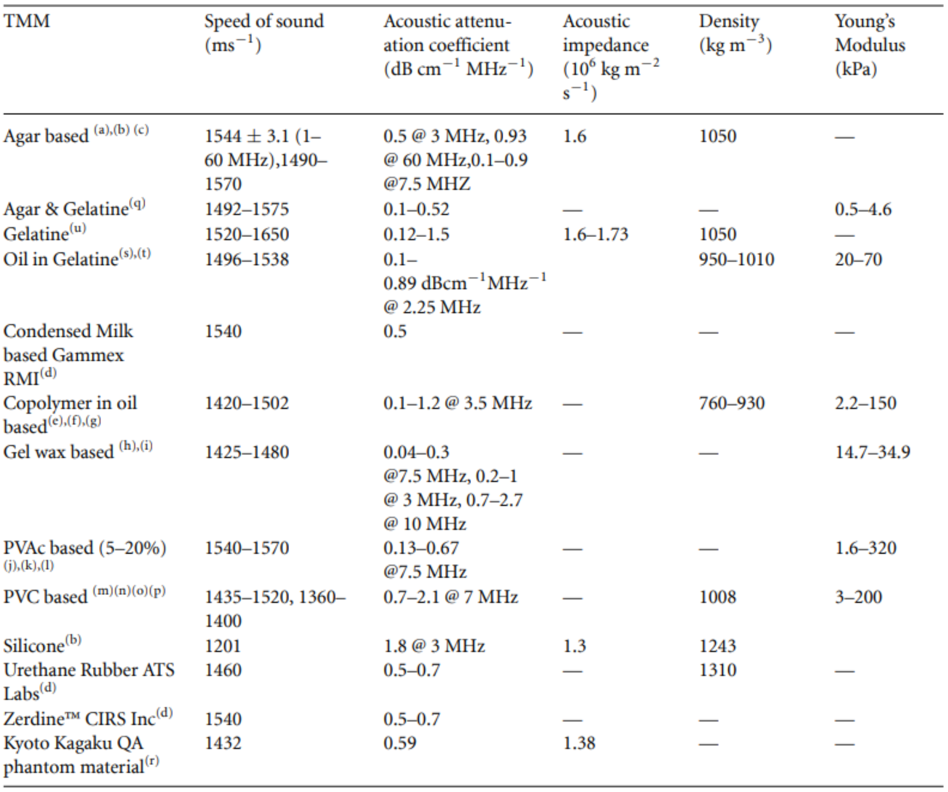

TMM	Speed of sound (ms^{-1})	Acoustic attenuation coefficient ($dB\ cm^{-1}\ MHz^{-1}$)	Acoustic impedance ($10^6\ kg\ m^{-2}\ s^{-1}$)	Density ($kg\ m^{-3}$)	Young's Modulus (kPa)
Agar based (a),(b) (c)	1544 ± 3.1 (1–60 MHz),1490–1570	0.5 @ 3 MHz, 0.93 @ 60 MHz,0.1–0.9 @7.5 MHZ	1.6	1050	—
Agar & Gelatine(q)	1492–1575	0.1–0.52	—	—	0.5–4.6
Gelatine(u)	1520–1650	0.12–1.5	1.6–1.73	1050	—
Oil in Gelatine(s),(t)	1496–1538	0.1–0.89 $dBcm^{-1}MHz^{-1}$ @ 2.25 MHz		950–1010	20–70
Condensed Milk based Gammex RMI(d)	1540	0.5	—	—	—
Copolymer in oil based(e),(f),(g)	1420–1502	0.1–1.2 @ 3.5 MHz	—	760–930	2.2–150
Gel wax based (h),(i)	1425–1480	0.04–0.3 @7.5 MHz, 0.2–1 @ 3 MHz, 0.7–2.7 @ 10 MHz	—	—	14.7–34.9
PVAc based (5–20%) (j),(k),(l)	1540–1570	0.13–0.67 @7.5 MHz	—	—	1.6–320
PVC based (m)(n)(o)(p)	1435–1520, 1360–1400	0.7–2.1 @ 7 MHz	—	1008	3–200
Silicone(b)	1201	1.8 @ 3 MHz	1.3	1243	
Urethane Rubber ATS Labs(d)	1460	0.5–0.7	—	1310	—
Zerdine™ CIRS Inc(d)	1540	0.5–0.7	—	—	—
Kyoto Kagaku QA phantom material(r)	1432	0.59	1.38	—	—

Figure 4.2: Acoustic and mechanical characteristics of common TMM for ultrasound application. Table by [37]

Polyvinyl Alcohol (PVA)

PVA TMMs are highly adaptable making it one of the most suitable materials to realize a muscle mimicking phantom. By modifying PVA concentrations and adjusting freeze-thaw cycles, their acoustic and mechanical characteristics can indeed be fine-tuned.

Copolymer in Oil

This material is notable for its consistent and repeatable properties, where adjusting component ratios can modify attenuation coefficients while retaining a stable sound speed. However, its sound speed is sensitive to temperature, which might limit its use in certain scenarios.

Polyvinyl Chloride (PVC)

PVC TMMs are versatile indeed adjusting softeners and additives allows for tailored sound speeds and attenuation coefficients, enabling them to emulate different tissues.

In summary, there's a diverse range of materials available for crafting muscle-like material. Each offers unique characteristics and can be tailored to resemble different tissues, equipping researchers and medical professionals with a comprehensive set of tools for reliably replicating human tissue.

4.3 Muscle mimicking material

After a comprehensive exploration of various materials suitable for fabricating a muscle phantom in ultrasound studies, this research elected to use Polyvinyl Chloride (PVC) as the primary material. PVC was chosen primarily for its acoustic properties, which are similar to those of human muscle, making it an ideal choice for mimicking muscle in our ultrasound investigations. Moreover, PVC is a durable material, with a lifespan of up to 100 years, ensuring the longevity of our phantom model. This contrasts with other materials like Polyvinyl Alcohol (PVA), which, although frequently employed in literature, does not offer the same longevity and ease of manufacture as PVC. The following sections of this chapter detail the fabrication process of the muscle-mimicking phantom using PVC, which aims to create a realistic and reliable model for the ultrasound wearable sensor tests. But first, the essential acoustic properties that the phantom must share with human muscle are presented.

4.3.1 Acoustic properties

The acoustic properties of a material refer to how sound waves interact with it. Key parameters include the speed of sound in the material, how much the material attenuates or absorbs sound, and the backscatter or reflection of sound waves from the material's surface.

Speed of sound

The speed of sound in a given medium is a fundamental acoustic property. It can be determined by measuring the time it takes for a sound signal to travel to a boundary within the medium and back. This technique involves a sample of known thickness, with the thickness represented by d as it is possible to observe in Figure 4.3. By emitting a sound signal at one boundary of the sample and measuring the time δt it takes for the signal to reach the other boundary and reflect back, we can compute the speed of sound c using the equation

$$c = \frac{2d}{\Delta t} \tag{4.1}$$

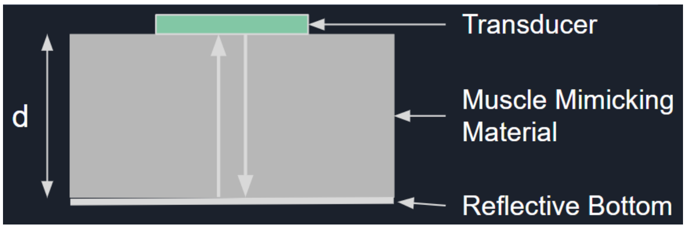

Figure 4.3: Measure of the speed of sound of a material. Illustration by Elizabeth Suitor

Attenuation

Attenuation, represented as α (f), is another important acoustic property that indicates the extent to which a medium absorbs sound waves, reducing their intensity. It can be measured by comparing the power spectrum of water,[Pw(f)], to the power spectrum after passing through the sample, Ps(f), at a fixed distance as illustrated in Figure 4.4. The thickness of the sample, represented as Δx, is also considered in this calculation. Using these values, the attenuation can be computed using the equation

$$\alpha(f) = \frac{10}{\Delta x} \log \frac{P_w(f)}{P_s(f)} \tag{4.2}$$

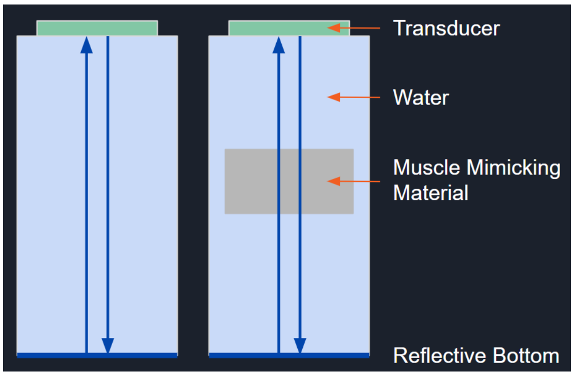

Figure 4.4: Measure of the attenuation of a material. Illustration by Elizabeth Suitor

Backscatter

Backscatter, defined as the reflection of waves upon encountering structures within a material, stands as a pivotal acoustic property. It's paramount to replicate this property accurately, making it our primary focus. To analyze backscatter and understand the speckle pattern of the phantom, we examine both the mean and standard deviation of pixel intensity in B-mode images of the phantom. Evaluating the pixel intensity across areas, as well as in horizontal and vertical orientations, offers a comprehensive insight into the speckle pattern.

4.3.2 Fabrication process

Our phantom fabrication process is anchored in established literature [38] [39], solidifying the credibility and efficacy of our methods. Furthermore, as we developed our unique recipe, we drew inspiration from Fromageau et al.'s 2007 PVA recipe [40], where they experimented with varying speckle material percentages to most accurately emulate muscle tissue.

Equipment

To produce the muscle-mimicking materials, specific instruments and materials are required. In Figure 4.5 it is possible to see the manufacturing site and the additive combined with PVC to enhance its resemblance to muscle tissue while below is a comprehensive list detailing all the components required to construct the phantom.

- Fume hood
- 1000 mL Beaker
- Thermometer
- Hot Plate
- Magnetic Stirrer
- Mold
- Mold Releaser
- Regular Liquid Plastic PVC Polymer
- Mineral Oil
- Graphite

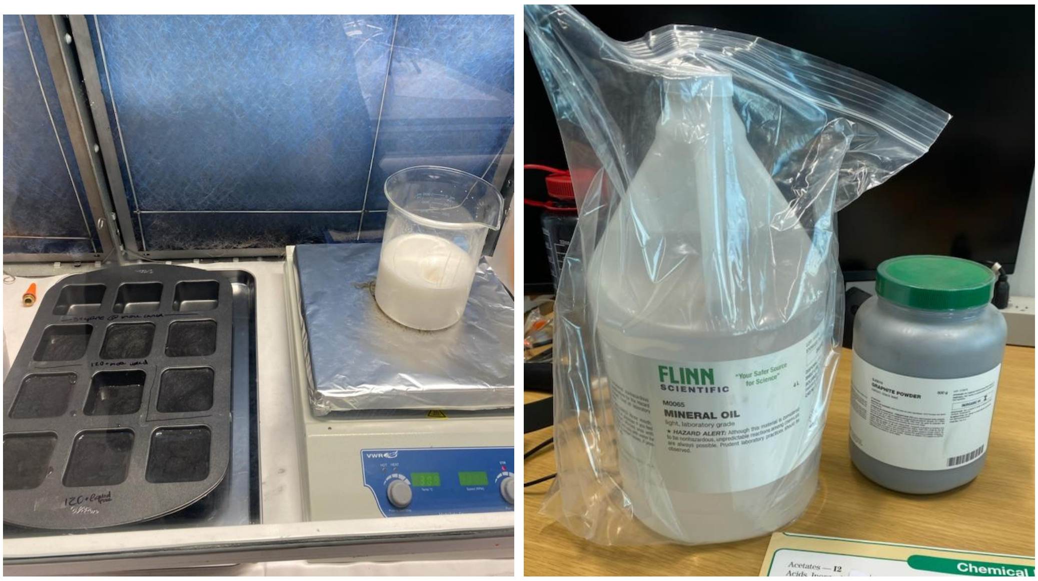

Figure 4.5: On the left is the fume hood with inside the hot plate, beaker, mold, and PVC solution while on the right the additive used

Process

The step-by-step process for fabricating the muscle-mimicking material is as follows:

1. Mix Regular Liquid Plastic PVC Polymer and Mineral Oil:
   Begin the process by placing the required amount of Regular Liquid Plastic PVC Polymer and Mineral Oil into the 1000 mL beaker. The mixing process should be carried out under a fume hood to ensure adequate ventilation. This is essential as some fumes may be released during the heating process.

2. Slowly Heat to Approximately 175C:
   With the mixture of Regular Liquid Plastic PVC Polymer and Mineral Oil in the beaker, place it on a hot plate and heat it gradually. Use a thermometer to monitor the temperature and ensure it reaches around 175C. Heating the material allows it to liquefy and become more manageable during the subsequent steps.

3. Add and Mix in Graphite:
   As the material begins to thicken and change from a milky white color to translucent, it is time to add the graphite. Graphite is a key component that imparts the muscle-like properties to the material. Slowly pour the graphite into the beaker while continuously stirring with the magnetic stirrer to ensure uniform distribution.

4. Remove from Heat and Pour into Mold:
   Once the material has reached the desired translucent consistency and the graphite is well mixed, remove the beaker from the hot plate to stop further heating. With caution, pour the mixture into the chosen mold.

5. Allow Cooling and Solidification:
   After pouring the material into the mold, let it cool naturally. Cooling and solidification may take some time, depending on the size and thickness of the material. It is crucial to allow sufficient cooling time to ensure the material retains its intended shape and properties.

6. Demold the Muscle Mimicking Material:
   Once the material has fully cooled and solidified, carefully remove it from the mold. Applying a mold release agent before pouring the material can aid in easy demolding.

The fabrication process produces an acoustic muscle-mimicking material that effectively replicates the speckle pattern of muscles using graphite. Its flexibility and characteristics make it well-suited for ultrasound applications. Although promising, further research is necessary to fully explore its potential and applications.

Benchtop Test Setup

In our benchtop test setup designed for muscle simulation, we aimed to replicate the horizontal motion of muscle beneath the skin. The benchtop test setup we employed to achieve this objective is depicted in Figure 4.6 on the left.

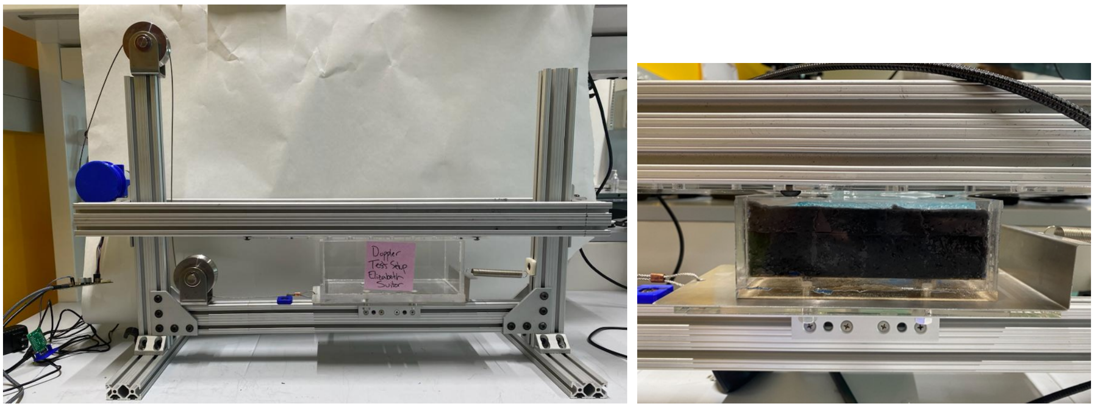

Figure 4.6: On the left the benchtop setup and on the right the phantom inside of the tank on the moveable cart

In the benchtop setup, a tank to contain the phantom was incorporated, which can be viewed in Figure 4.6 on the right. The tank was positioned on a moveable cart which on one side was anchored to the structure through a spring, while the opposite side was attached to a wheel. This wheel was set in motion by a DC motor equipped with an encoder. This configuration not only ensured controlled movement of the phantom but also provided motion tracking, with the encoder serving as a reliable reference for movement accuracy.

To capture ultrasound signals efficiently, a linear array transducer was positioned on the surface of the tissue-mimicking material, with a gentle indentation to optimize signal reception. Additionally, ultrasound gel was applied to the surface of this material, ensuring effective index matching and enhancing signal transmission as previously explained. Figure 4.7 showcases the complete Benchtop Test Setup. At the rear, the structure housing the phantom tank is visible. To the left, the computer designated to control the motor, while the right side features a computer to analyze the received ultrasound signal.

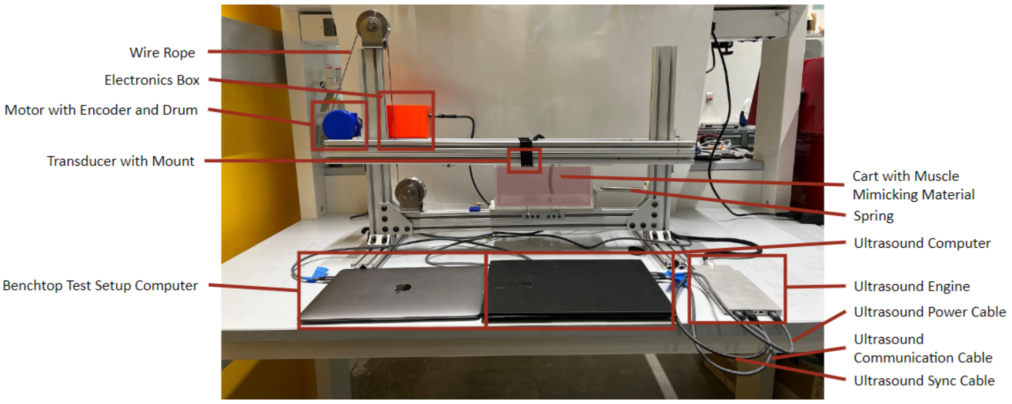

Figure 4.7: Complete Benchtop Test Setup. Illustration by Elizabeth Suitor

4.3.3 Results

To identify the optimal recipe to replicate muscle properties, we conducted experiments considering various factors: graphite percentages, pouring speeds, temperatures, degassing processes, and stirring techniques. Initially, we planned to explore graphite concentrations ranging from 1% to 4% (Table 4.1) to ascertain its impact on the speckle pattern of the phantom. However, as we will elaborate later, the full exploration proved unnecessary.

Material	**Mixture 1**	**Mixture 2**	**Mixture 3**	**Mixture 4**
Regular Liquid Plastic PVC Polymer	91.1%	90.2%	89.2%	88.3%
Mineral Oil	7.9%	7.8%	7.8%	7.7%
Graphite	1.0%	2.0%	3.0%	4.0%

Table 4.1: Initial mixture plan

Muscle reference Firstly, to set a clear target, we conducted ultrasound measurements on a real muscle. In Figure 4.8 on the left it is possible to see a B-mode image of a leg. The first layer is the skin, then there is fat, and then the muscle. On the muscle, a red rectangle surrounding the Region Of Interest (ROI) of 15x5 mm [41] is shown. Specifically, from this image, we examined the pixel intensity within the ROI across all video frames and it is possible to see the result in Figure 4.8 on the right. Pixel intensity values are represented using 8 bits, which means the maximum intensity, corresponding to white, is set at 255.
Additionally, we analyzed the distribution of the intensity across columns and rows to discern if there was some sort of pattern, and the results are shown in Figure 4.9. From these latter pictures, it is possible to understand that no pattern is expected except an almost constant mean intensity along columns and rows in the ROI.

PVC phantom with 1% graphite Our first experiment, as mentioned earlier, involved a mixture with 1% graphite content. Figure 4.10 displays a B-mode image of the phantom. As in the previous case, the red rectangle in the figure delineates the studied Region Of Interest (ROI). The results of the pixel intensity analysis are reported in Figure 4.11. As it is possible to see, when compared to the previous muscle analysis, it is evident that the mean pixel intensity is marginally lower, for this reason, we proceeded with the next mixture.

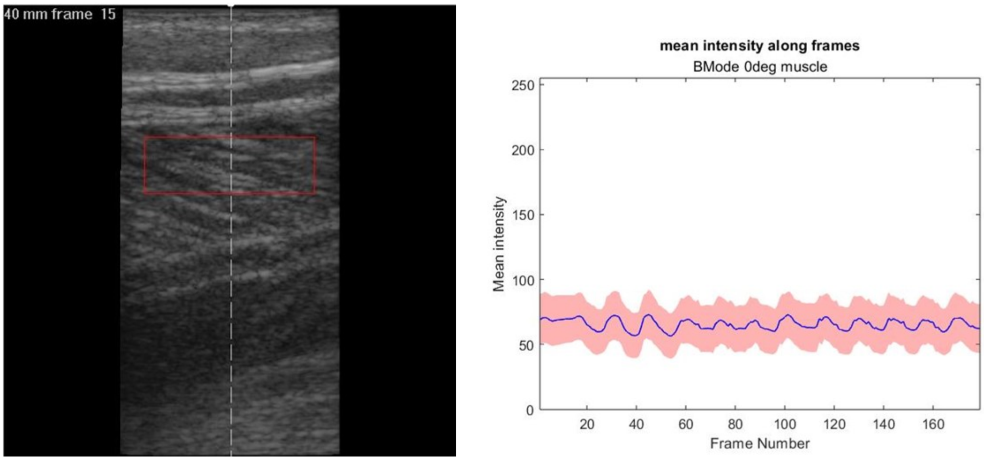

Figure 4.8: On the left is a B-mode image of a leg and on the right the pixel intensity study inside the ROI

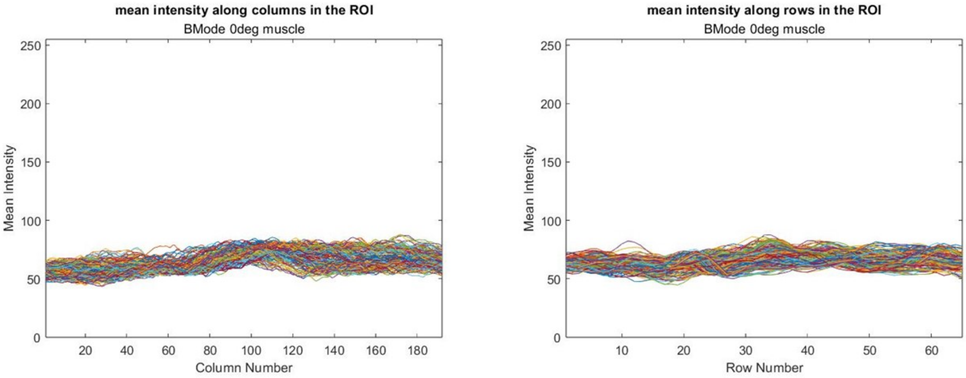

Figure 4.9: Pixel intensity study of a real muscle along columns and rows within the ROI

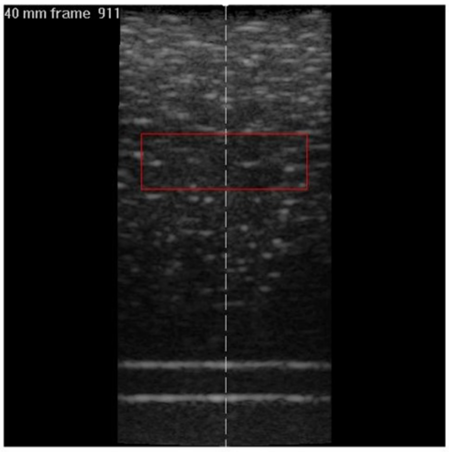

Figure 4.10: Mixture with 1% graphite

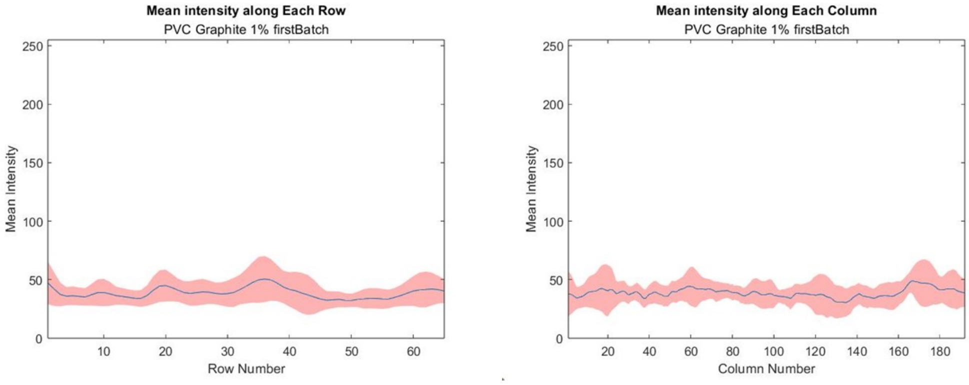

Figure 4.11: Analysis of pixel intensity, mixture with 1% graphite

PVC phantom with 3% graphite We next tested a mixture comprising PVC phantom with 3% graphite content. Notably, the ultrasound image of this phantom (Figure 4.12) appeared darker compared to the 1% graphite mixture. This darkening could be attributed to bubble presence or potentially due to increased attenuation.

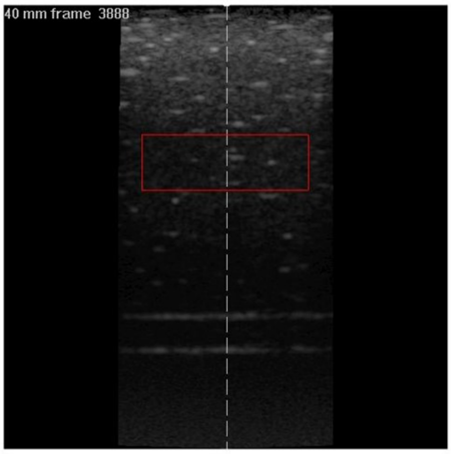

Figure 4.12: Mixture with 3% graphite

An analysis of pixel intensity across rows and columns shown in Figure 4.13 revealed a lower mean intensity than the previous mixture. Thus, increasing the graphite percentage might not be the optimal approach to create a muscle-mimicking material.

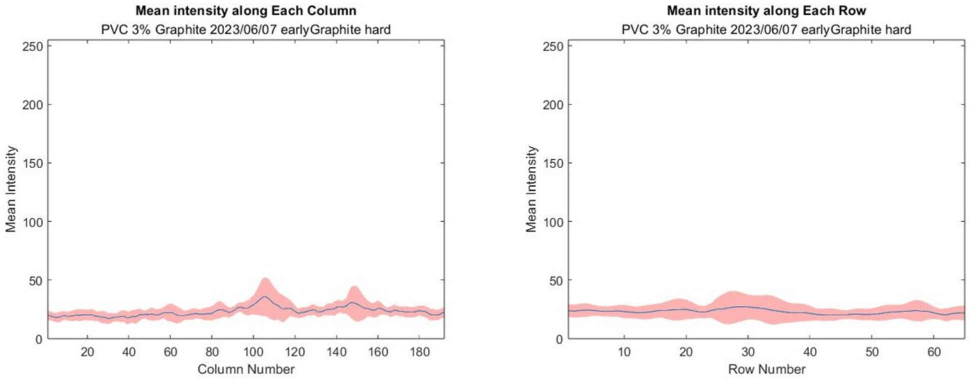

Figure 4.13: Analysis of pixel intensity, mixture with 3% graphite

PVC phantom with Psyllium For our third mixture, we opted for Psyllium as the backscattering material, replacing graphite. Notably, Psyllium had been previously utilized in our initial gelatin phantom creations that were later set aside because gelatin goes bad in 3 days and so a gelatin phantom could not be a long term solution. Hence, we sought to investigate Psyllium behavior further. Figure 4.14 presents three distinct B-mode images of PVC phantoms. Moving from left to right, these phantoms contain 1%, 2%, and 3% psyllium, respectively.

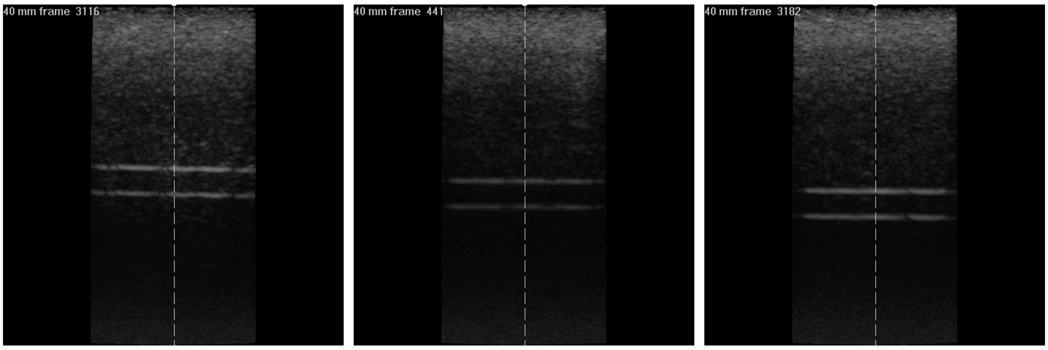

Figure 4.14: Mixture with 1%,2% and 3% psyllium

Upon analysis, the impact of Psyllium appears minimal. Varying its concentration does not seem to significantly adjust the phantom's behavior to mimic muscle tissue. Thus, Psyllium might not be an ideal choice as a backscattering material for a PVC phantom.

PVC phantom with 0.5% graphite and 2.5% psyllium Given that psyllium alone did not significantly influence the phantom's properties, we explored a combination of psyllium and graphite to evaluate the resultant behavior. Figure 4.15 displays the B-mode image of this composite phantom.

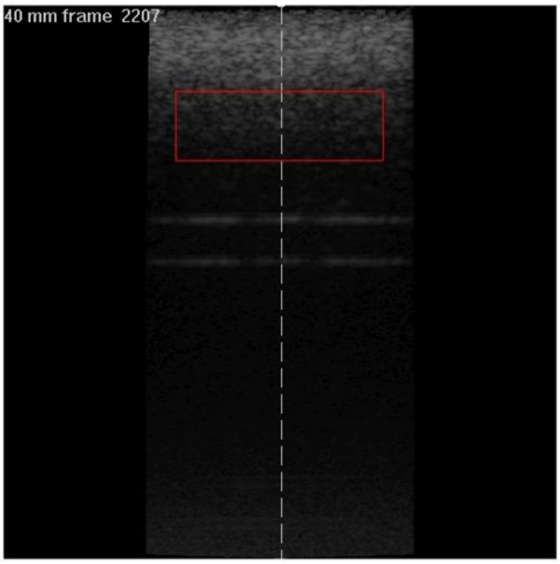

Figure 4.15: Mixture with 0.5% graphite and 2.5% psyllium

As observed in Figure 4.16, the mean pixel intensity within the ROI declines rapidly. Since this behavior is not characteristic of human muscle tissue, this combination was subsequently deemed unsuitable.

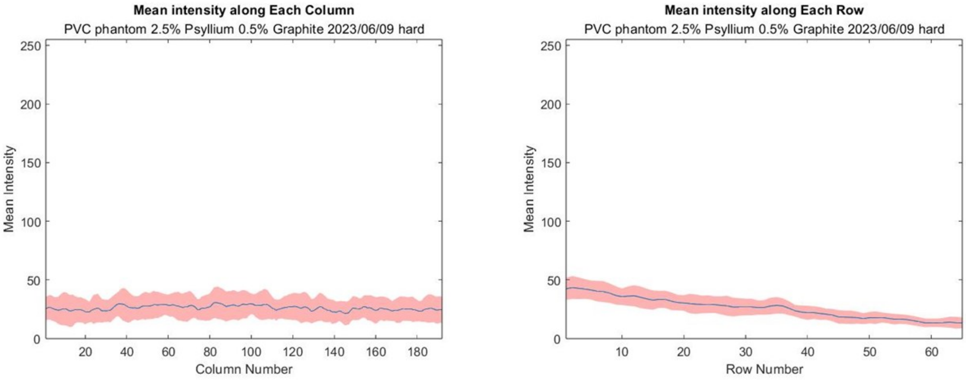

Figure 4.16: Analysis of pixel intensity, mixture with 0.5% graphite and 2.5% psyllium

Muscle vs PVC graphite phantom Having set aside the PVC with Psyllium option, we were left to consider PVC phantoms with graphite percentages of 1% and 3%. Figure 4.17 shows the muscle tissue with the two aforementioned phantoms. Notably, the 3% graphite PVC phantom exhibits greater attenuation compared to human muscle. Consequently, the 1% graphite phantom emerged as the most promising PVC variant evaluated thus far. This has piqued our interest in examining a phantom with 0.5% graphite content.

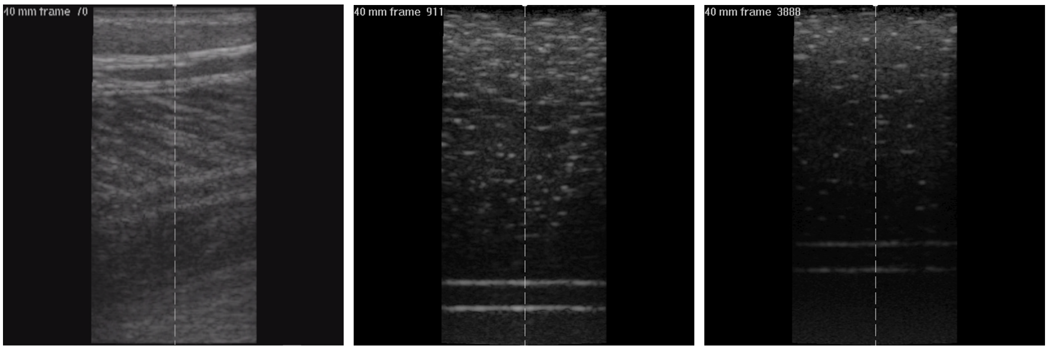

Figure 4.17: From left to right: B-mode image of muscle tissue, 1% graphite phantom and 3% graphite phantom

PVC phantom with 0.5% graphite Based on our earlier investigations, the ROI has been shifted to a higher position in the image as it is possible to observe in Figure 4.18, aiming to enhance the mean pixel intensity within the ROI. Observing Figure 4.19, it's clear that this configuration given by a higher position ROI and 0.5% graphite presents the most promising muscle-mimicking material to date. Thus, we've resolved to adopt this graphite concentration for subsequent studies.

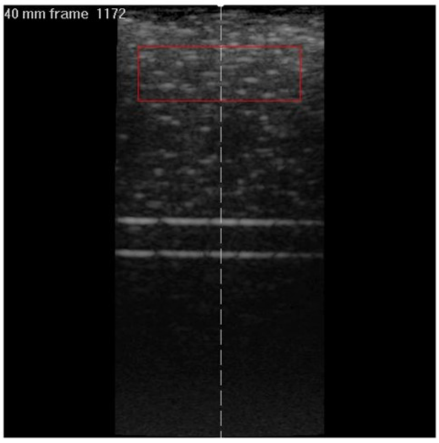

Figure 4.18: Mixture with 0.5% graphite

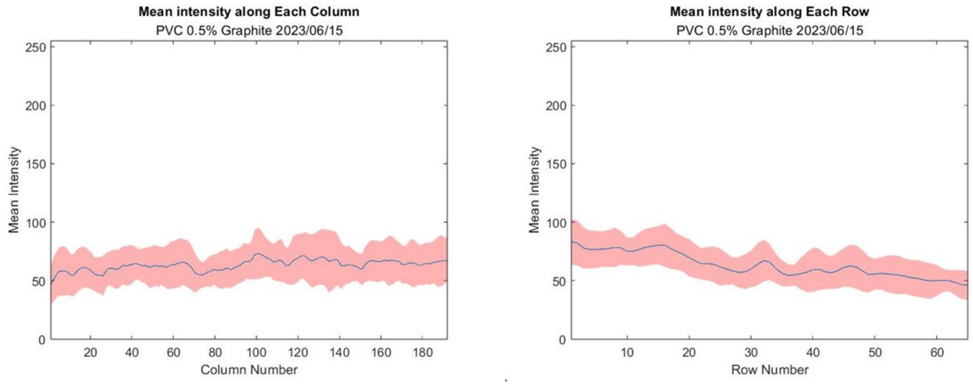

Figure 4.19: Analysis of pixel intensity, mixture with 0.5% graphite

PVC muscle phantom

Figure 4.20 displays the resulting phantom on the left, alongside a real muscle. As mentioned earlier, this phantom is characterized by a 0.5% graphite content. The distinct white line, that is possible to see in the PVC phantom, arises from the backer's limited size, leading us to craft two separate phantoms and place them on top of each other to fill the cart in the benchtop setup.

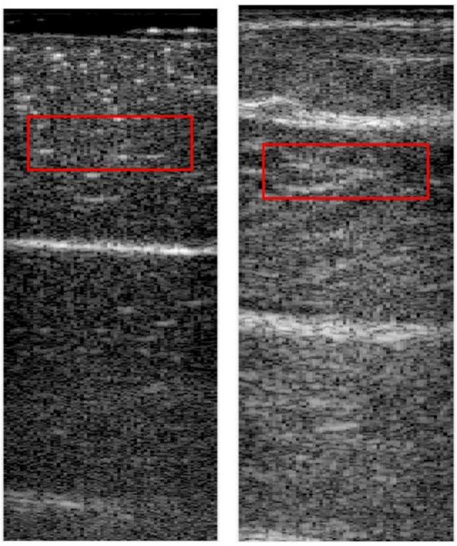

Figure 4.20: On the left the final PVC phantom with 0.5% graphite and on the right a human muscle

Phantom Building on the phantom depicted in Figure 4.20, we conducted four distinct measurements, specifically focusing on the mean intensity and standard deviation across the frames of the recorded B-mode videos, as illustrated in 4.21.

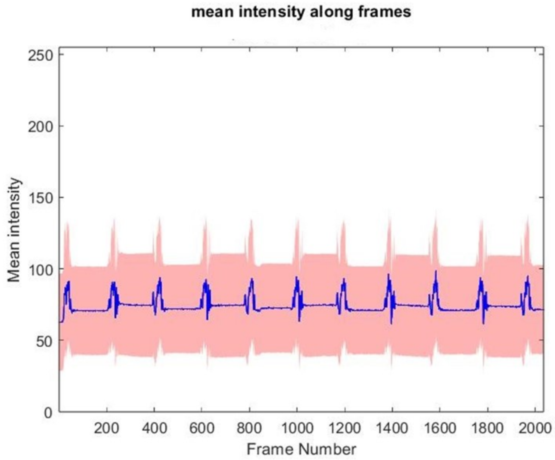

Figure 4.21: Pixel intensity analysis, muscle mimicking material

We then derived the overall average intensity and average standard deviation inside of the ROI for each one of the measurements, details of which are presented in Table 4.2.

DataSet	Mean Intensity	Mean St.Dev
01	74.38	34.37
02	74.34	34.11
03	73.65	34.05
04	73.24	33.29
ALL	73.90	33.96

Table 4.2: Intensity analysis of 4 B-mode videos of the phantom

In Vivo Following the phantom analysis, in vivo studies were undertaken. Specifically, B-mode videos of the gastrocnemius muscle were collected from 10 participants as they performed the movement depicted in Figure 4.22.

The gathered data varied widely: some results appeared markedly different from the phantom, as illustrated in Figure 4.23, while others exhibited behavior closely resembling the phantom, as showcased in Figure 4.24.

The intensity data derived from the in vivo study can be found in Table 4.3.

Figure 4.22: Movement computed by the participants. Image by [42]

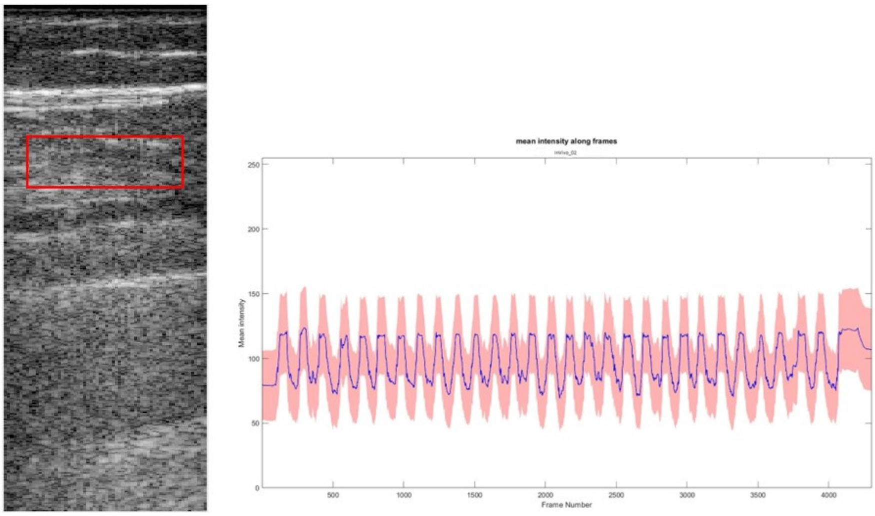

Figure 4.23: B-mode image and intensity analysis of participant #2

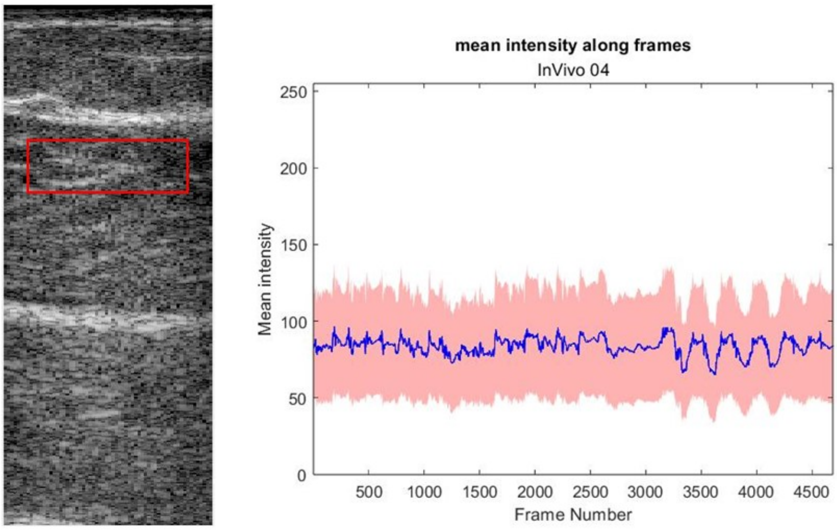

Figure 4.24: B-mode image and intensity analysis of participant #4

Participant	Mean Intensity	Mean St.Dev
01	91.78	31.40
02	97.82	29.36
03	109.51	36.39
04	83.66	35.75
05	51.91	34.21
06	68.99	40.75
07	71.96	33.91
08	44.93	29.89
09	85.09	32.91
10	78.96	37.20
ALL	78.49	34.18

Table 4.3: Intensity analysis of 10 B-mode videos of real muscle

Phantom vs In Vivo Observing Figure 4.25, there isn't a significant difference between the data from the muscle-mimicking material and the in vivo results. Notably, the in vivo mean intensity of different participants appears to fluctuate around the phantom's mean intensity value.

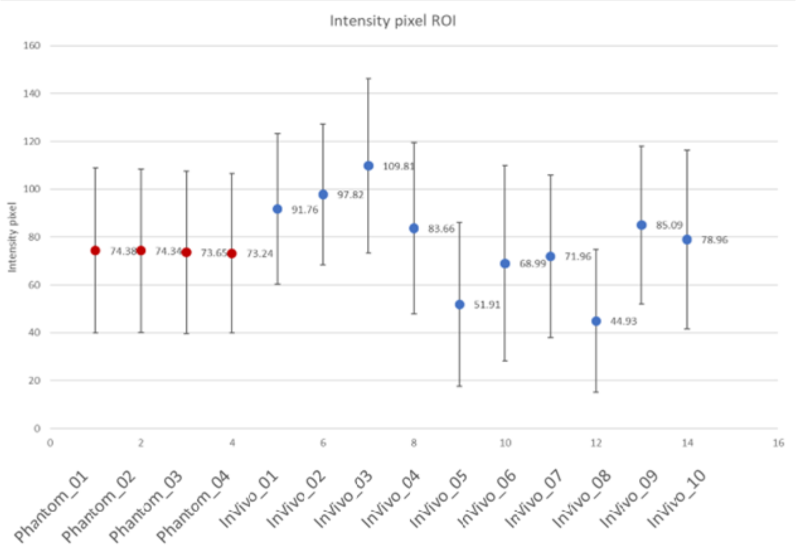

Figure 4.25: Mean intensity and standard deviation of B-mode videos of phantom in red and real muscle in blue

When we shift our focus from individual data sets to the overall mean value, as presented in Figure 4.26, the similarity between the two data groups becomes more pronounced and compelling.

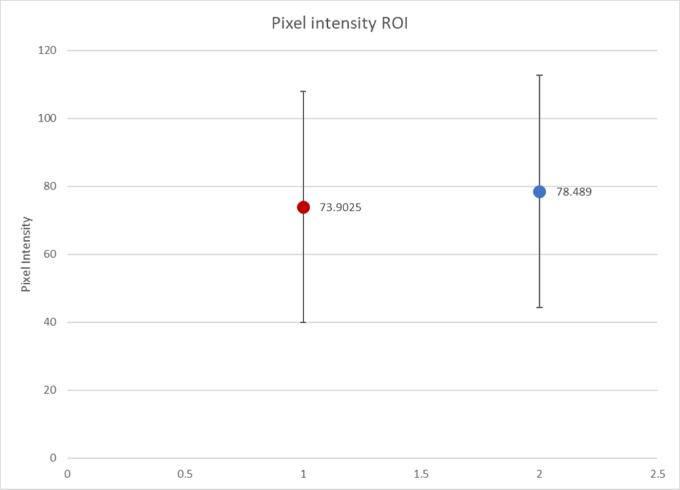

Figure 4.26: Mean intensity and standard deviation of phantoms in red and blue of real muscle

Statistical analysis In order to validate the coherence of the data collected from the fabricated phantom as compared to the muscular data, an exhaustive statistical analysis was carried out. This included the use of two critical statistical tests, namely the Kolmogorov-Smirnov test and the Mann-Whitney-Wilcoxon non-parametric test.

The Kolmogorov-Smirnov test is a non-parametric method used to determine whether two sets of data are significantly different from each other. This was applied to evaluate the distribution of the collected data. The test results indicated that the data did not conform to a normal distribution, providing us with an understanding of the underlying statistical characteristics of the data set.

The Mann-Whitney-Wilcoxon test, another non-parametric method, was subsequently employed. This test is used to compare two independent samples to determine if they come from the same distribution or, equivalently, from identical populations. In this case, it was used to discern any significant differences between the two sets of data: the data from the fabricated phantom and the muscular data. The results indicated no significant difference between these two data sets, lending confidence to the accuracy and consistency of using the phantom to tune the algorithm to measure muscle velocity.

4.4 Optical flow

Optical flow is a method used to measure the motion of objects within images or videos [43]. It operates on the idea of a flow field, illustrating the pixel transitions over a duration in visual data. This approach aids in determining the velocity and trajectory of individual pixel movements.

This method is widely employed for tasks like object tracking, scene comprehension, and action recognition. At the heart of optical flow is the tracking of changes in pixel clusters as images change. For example, when a car moves across an image, the pixels associated with that car will mirror its trajectory and velocity. Analyzing these pixel changes allows us to infer the direction and speed of the car's movement.

A fundamental principle in this context is brightness constancy, which suggests that the brightness of a pixel in visuals stays the same over a period. This principle is the foundation of the optical flow's prediction method, which aims to anticipate the future brightness of pixels.

Consider a pixel with certain characteristics, like its color values, at a moment 't'. A bit later, this pixel might be elsewhere but retains its characteristics. This shift is what the flow field anticipates and is the central assumption of optical flow.

For example, if there's a white dot in a photo at a certain moment t, it might shift to another spot in the next moment t+dt. To measure the pixel's movement, we refer to the optical flow displacement vector. In this context, the vector is [dx,dy]. The new pixel's location is determined by taking the original pixel's spot and adding this vector as it is possible to see in Figure 4.27.

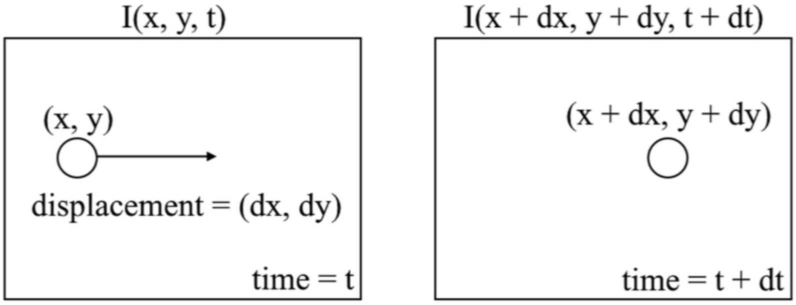

Figure 4.27: Tracking of the pixel position to determine its velocity

Since the pixel is always the same and so its brightness remains the same, it is possible to express the constant intensity assumption, which is at the base of optical flow, as

$$I(x, y, y) = I(x + \delta x, y + \delta y, t + \delta t) \tag{4.3}$$

Using mathematical approaches, it is possible to derive the Optical Flow equation which allows us to calculate the image gradients and the gradient over time.

$$f_x u + f_y v + f_t = 0 \tag{4.4}$$

$$f_x = \frac{\partial f}{\partial x}; f_y = \frac{\partial f}{\partial y} \tag{4.5}$$

$$u = \frac{dx}{dt}; v = \frac{dy}{dt} \tag{4.6}$$

Yet, there are some unknowns in this equation for this reason is not possible to solve the problem directly. As a consequence, various techniques have been introduced to overcome the issue, in particular, the one we planned on using is the Lucas-Kanade approach which will be later introduced. Other methods, such as Buxton-Buxton and Horn-Schunck, also exist.

Lastly, there are two main kinds of optical flow: Sparse and Dense. Sparse focuses on certain key parts of a visual as it is possible to see in Figure 4.28 on the right, while Dense looks at every pixel shown in Figure 4.28 on the left. Though Dense gives more detail, it requires more computer power and is slower.

Figure 4.28: Sparse optical flow on the right and dense optical flow on the left[44]

4.4.1 Implementing sparse optical flow

To optimize computing resources and focus on the essential details of our study, we chose sparse optical flow. Our videos primarily capture the movement of muscles and don't require intricate detailing. Sparse optical flow, which emphasizes select pixels, aligns perfectly with our needs, ensuring efficient tracking of motion vectors. In order to analyze our videos the affine optic flow model on Matlab [45] was suggested.

The first step in order to use the algorithm to study the velocity of muscle was to tune the parameters of the algorithm based on the ground truth velocity that we were able to obtain thanks to the benchtop test setup.

Tuning of the optical flow algorithm

First, we incorporated a Butterworth filter into the algorithm with a cut-off frequency of 10Hz. This adjustment was crucial to address excessive noise in our data and this frequency was used since it is commonly used in biological measurements to counteract noise in the results. Subsequently, the model's parameters have been adjusted, and the optimal settings obtained are illustrated in Figure.

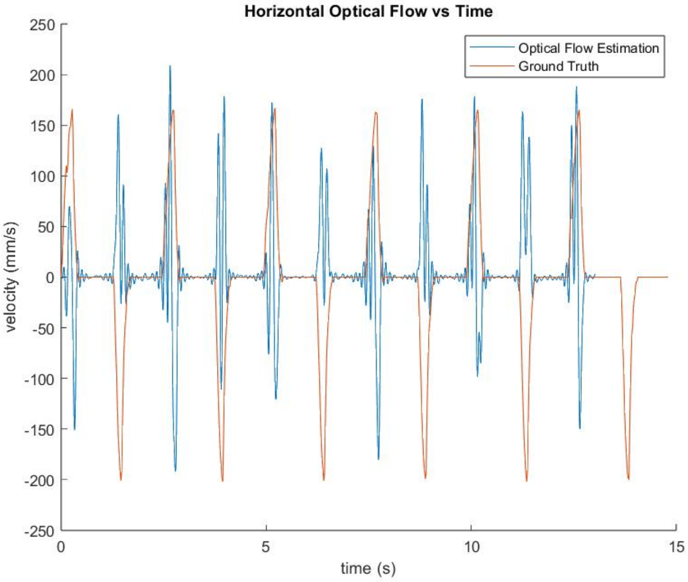

Figure 4.29: Measured phantom velocity with optical flow vs ground truth

From the beginning, we recognized the constraints of optical flow in precisely determining muscle velocity. While the necessity for case-specific adjustments is a recognized shortcoming of optical flow, we are confident that optimizing the algorithm's parameters can further improve its performance but due to time constraints, we were not able to do it. Additionally, to correct the cart's imprecise velocity direction assumption, we can enhance the motor's code execution, ensuring a smoother transition in the phantom's directional shift.

4.5 Doppler ultrasound method

Doppler ultrasound, traditionally recognized for its proficiency in measuring blood flow, is now being explored for its potential in gauging muscle velocity.
Doppler ultrasound is a non-invasive diagnostic technique that harnesses the Doppler effect to measure the velocity of moving structures within the body. When the ultrasound's emitted sound waves encounter movement, such as that of a muscle as it is possible to see in Figure 4.30, they reflect back with a modified frequency, indicative of the velocity of the movement.

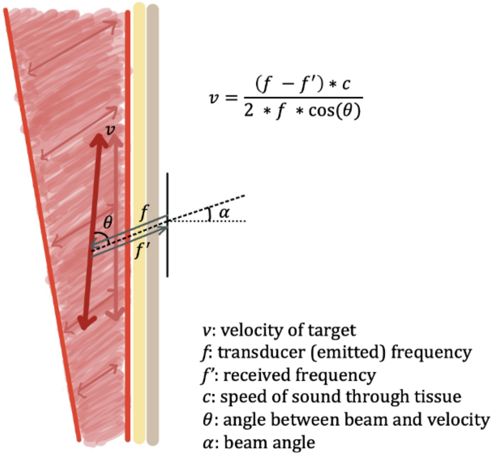

Figure 4.30: The doppler effect. Illustration by Elizabeth Suitor

Using a transducer placed on the skin above the target area, as the sound waves rebound upon detecting muscle movement, the ultrasound device interprets the reflected waves, deducing the muscle's speed and direction of movement. This information is typically visualized in real-time on a monitor, with color intensity representing the speed of movement and varying colors indicating different directions (Color Doppler imaging). While its primary application has been in assessing blood flow, the potential of Doppler ultrasound in characterizing muscle velocity is an exciting frontier, promising new insights in the medical field.

4.6 Doppler vs Optical Flow

The Doppler ultrasound method, when compared to optical flow, presents several advantages, especially when the objective is to measure muscle velocity. Traditionally, Doppler ultrasound has been a trusted tool in the medical field, primarily for gauging blood flow. Its precision, real-time feedback, and non-invasive nature make it a preferred choice for many clinicians. On the other hand, optical flow, while valuable in certain applications, has its limitations, particularly when it comes to detecting muscle velocity. One of the primary challenges with optical flow is the need for case-specific tuning, which can be time-consuming and may not always yield consistent results across different scenarios. Additionally, optical flow can sometimes struggle with noisy data, requiring additional filtering or processing steps. In contrast, Doppler ultrasound provides direct, real-time measurements without the need for extensive post-processing. Furthermore, Doppler ultrasound is inherently designed to capture internal body movements, making it more suited for tasks like measuring muscle velocity. As we look to the future, our aim is to substantiate the superiority of the Doppler method over optical flow. Through rigorous testing and analysis, we hope to demonstrate that, for muscle velocity measurements, Doppler ultrasound stands out as the more reliable and efficient choice.

Chapter 5

Conclusions

In conclusion, this thesis puts forth a structured approach to the design of piezoelectric transducers for ultrasound applications, strategically integrating the strengths of the KLM and finite element models. In the initial stage of design, the KLM model, known for its low computational requirements, is invaluable for rapidly identifying key parameters that guide the transducer design. By doing so, it provides a quick and efficient method for sifting through various design possibilities.

Once the crucial parameters have been isolated, the finite element model allows for more exhaustive and detailed design optimization. This model is especially well-suited for diving deep into aspects such as complex geometries and material anisotropies, factors that may be glossed over by the KLM model. By employing this two-step methodology, we achieve a judicious balance between computational efficiency and design robustness, culminating in a highly optimized and reliable transducer.

Moreover, our research into wearable sensors for assessing skeletal muscle kinematics accentuates the importance of creating a test phantom for refining the optical flow algorithm. Due to time constraints, a full-scale comparison with the Doppler method was not feasible, but preliminary findings are quite suggestive. Doppler ultrasound stands out for its precision, real-time capabilities, and non-dependency on tissue structure, making it a strong candidate for clinical applications. Conversely, the optical flow method has its limitations, such as the need for case-specific fine-tuning and susceptibility to noisy data, which often necessitates further post-processing steps. As next steps, we are committed to a more thorough validation of Doppler ultrasound's superiority in measuring muscle velocity.

Bibliography

[1] Hongjie Hu, Hao Huang, Mohan Li, Xiaoxiang Gao, Lu Yin, Ruixiang Qi, Ray S. Wu, Xiangjun Chen, Yuxiang Ma, Keren Shi, Chenghai Li, Timothy M. Maus, Brady Huang, Chengchangfeng Lu, Muyang Lin, Sai Zhou, Zhiyuan Lou, Yue Gu, Yimu Chen, Yusheng Lei, Xinyu Wang, Ruotao Wang, Wentong Yue, Xinyi Yang, Yizhou Bian, Jing Mu, Geonho Park, Shu Xiang, Shengqiang Cai, Paul W. Corey, Joseph Wang, and Sheng Xu. A wearable cardiac ultrasound imager. *Nature*, 2023. DOI : 10.1038/s41586-022-05498-z.

[2] Xingchen Yang, Zhenfeng Chen, Nalinda Hettiarachchi, Jipeng Yan, and Honghai Liu. A wearable ultrasound system for sensing muscular morphological deformations. *IEEE Transactions on Systems, Man, and Cybernetics: Systems*, 2021. DOI : 10.1109/TSMC.2019.2924984.

[3] Dominic James Farris and Gregory S. Sawicki. Human medial gastrocnemius force-velocity behavior shifts with locomotion speed and gait. *Proceedings of the National Academy of Sciences*, 2012. DOI : 10.1073/pnas.1107972109.

[4] Richard W. Nuckols, Krithika Swaminathan, Sangjun Lee, Louis Awad, Conor J. Walsh, and Robert D. Howe. Automated detection of soleus concentric contraction in variable gait conditions for improved exosuit control. In *2020 IEEE International Conference on Robotics and Automation (ICRA)*, 2020. DOI : 10.1109/ICRA40945.2020.9197428.

[5] R. W. Nuckols, S. Lee, K. Swaminathan, D. Orzel, R. D. Howe, and C. J. Walsh. Individualization of exosuit assistance based on measured muscle dynamics during versatile walking. *Science Robotics*, 2021. DOI : 10.1126/scirobotics.abj1362.

[6] *Twomey Consulting, LLC.* url : https://www.twomeyconsulting.com/learn/ultrasound.

[7] Jim Stewart. WTF (Wireless Technology Fundamentals): Wave Mechanics II. *EEWeb*, 2018. url : https://www.eeweb.com/wtf-wireless-technology-fundamentals-wave-mechanics-ii/.

[8] Alexis Salerno and Sarah B. Murthi. *Obtaining, Interpreting, and Using Echo.* Springer International Publishing, 2021. DOI : 10.1007/978-3-030-74687-21.

[9] Ultrasound 101 - Part 1: Transducers. *123 Sonography*, 2022. url: https://123sonography.com/blog/ultrasound-101-part-1-transducers.

[10] Center for Devices Health and Radiological. Ultrasound imaging. *FDA*, 2023. url: https://www.fda.gov/radiation-emitting-products/medical-imaging/ultrasound-imaging.

[11] I. M. V. Imaging and Site Administrator. The A, B, M Ultrasound Modes Explained. *IMV Imaging*, 2023. url: https://www.imv-imaging.com/en/2023/04/the-a-b-ms-ultrasound-modes-explained/.

[12] Aria Ashir, Saeed Jerban, Victor Barrere, Yuanshan Wu, Sameer B. Shah, Michael P. Andre, and Eric Y. Chang. Skeletal Muscle Assessment Using Quantitative Ultrasound: A Narrative Review. *Sensors*, 2023. DOI : 10.3390/s23104763.

[13] Ultrasound. *National Institute of Biomedical Imaging and Bioengineering*, 2016. url : https://www.nibib.nih.gov/science-education/science-topics/ultrasound.

[14] Marti Rae. Vascular and Ultrasound - Enterprise Ultrasound, 2015. url: https://enterpriseultrasound.com/vascular-and-ultrasound/.

[15] Pierre C. Wong. *Science of Ultrasound and Echocardiography.* 2021. DOI: https://doi.org/10.1007/978-3-030-57193-11.

[16] Rachael Nightingale. Ultrasound transducer. *Radiopaedia.* url: https://radiopaedia.org/articles/ultrasound-transducer.

[17] S Sadia Nimra Zahra Fatima HM Fayzan Shakir ZA Rehan Sadia Afzal, Muhammad Zahid. Ultrasound Hydrogel: A Review on Materials and Method. *Journal of Modern Polymer Chemistry and Materials*, 2022. DOI = 10.53964/jmpcm.2022002.

[18] You Ling. What is piezoelectric ceramics? *HE-SHUAI*, 2023. url: https://www.he-shuai.com/what-is-piezoelectric-ceramics/.

[19] M. A. Fraga, H. Furlan, R. S. Pessoa, and M. Massi. Wide bandgap semiconductor thin films for piezoelectric and piezoresistive mems sensors applied at high temperatures: an overview. *Microsystem Technologies*, 2014. DOI: 10.1007/s00542-013-2029-z.

[20] R. Krimholtz, D.A. Leedom, and G.L. Matthaei. New equivalent circuits for elementary piezoelectric transducers. *Electronics Letters*, 1970. DOI: 10.1049/el:19700280.

[21] Stewart Sherrit, Sean P. Leary, Benjamin P. Dolgin, and Yoseph Bar-Cohen. Comparison of the Mason and KLM equivalent circuits for piezoelectric resonators in the thickness mode. *IEEE Ultrasonics Symposium. Proceedings. International Symposium*, 1999. DOI: 10.1109/ULTSYM.1999.849139.

[22] Siqi Ji, Hamed Esmaeilzadeh, Junwei Su, Sheree Pagsuyoin, and Hongwei Sun. Novel analysis of a micropillar coupled acoustic wave sensor. *Sensors and Actuators Reports*, 2021. DOI: 10.1016/j.snr.2021.100034.

[23] 3.19: Quarter-Wavelength Transmission Line. *Physics LibreTexts*, 2020. url: https://phys.libretexts.org/Bookshelves/Electricity_and_Magnetism/Book%3-A_Electromagnetics_I_(Ellingson)/03%3ATransmissionLines/3.19%3A_Quarter-WavelengthTransmission_Line.

[24] C.S. Desilets, J.D. Fraser, and G.S. Kino. The design of efficient broad-band piezoelectric transducers. *IEEE Transactions on Sonics and Ultrasonics*, 1978. DOI : 10.1109/T-SU.1978.31001.

[25] H.J. Fang, Y. Chen, C.M. Wong, W.B. Qiu, H.L.W. Chan, J.Y. Dai, Q. Li, and Q.F. Yan. Anodic Aluminum Oxideâepoxy composite acoustic matching layers for ultrasonic transducer application. *Ultrasonics*, 2016. DOI : 10.1016/j.ultras.2016.04.003.

[26] Vivek T. Rathod. A review of acoustic impedance matching techniques for piezoelectric sensors and transducers. *Sensors*, 2020. DOI : 10.3390/s20144051.

[27] Ke Zhu, Jinpeng Ma, Xudong Qi, Bingzhong Shen, Yang Liu, Enwei Sun, and Rui Zhang. Enhancement of ultrasonic transducer bandwidth by acoustic impedance gradient matching layer. *Sensors*, 2022. DOI : 10.3390/s22208025.

[28] Piezoacoustic transducer. *COMSOL Multiphysics.*
url : https://www.comsol.com/model/piezoacoustic-transducer-1477.

[29] COMSOL Multiphysics® v. 6.1. *COMSOL Multiphysics, Burlington, MA*, 1998. url : https://www.comsol.com/.

[30] Materials technical data (typical values), 2020.
URL: https://support.piezo.com/article/62-material-propertiespiezo.

[31] Morgan Advanced Materials. Typical properties. 2009. url: http://www.morganelectroceramics.com/resources/piezo-ceramictutorials-/typical-properties/.

[32] Ltd. APC International. Physical and piezoelectric properties of APC materials. 2020. url : https://www.americanpiezo.com/apc-materials/physical-piezoelectric-properties.html.

[33] Kyle Richard Wilt. *Experimentation and modeling of piezoelectric-based ultrasonic acoustic-electric channels*. PhD thesis, Rensselaer Polytechnic Institute, Troy, NY, 2012. url : https://hdl.handle.net/20.500.13015/3561.

[34] Jason R. Franz and Darryl G. Thelen. Imaging and simulation of achilles tendon dynamics: Implications for walking performance in the elderly. *Journal of Biomechanics*, 2016. DOI : 10.1016/j.jbiomech.2016.04.032.

[35] L. Nuri, S. J. Obst, R. Newsham-West, and R. S. Barrett. Regional three-dimensional deformation of human achilles tendon during conditioning. *Scandinavian Journal of Medicine Science in Sports*, 2017. DOI : 10.1111/sms.12742.

[36] Steven J. Obst, Rod S. Barrett, and Richard Newsham-West. Immediate effect of exercise on achilles tendon properties: Systematic review. *Medicine Science in Sports Exercise*, 2013. DOI : 10.1249/MSS.0b013e318289d821.

[37] Conor K McGarry, Lesley J Grattan, Aoife M Ivory, Francesca Leek, Gary P Liney, Yang Liu, Piero Miloro, Robba Rai, Andrew Robinson, Albert J Shih, Bajram Zeqiri, and Catharine H Clark. Tissue mimicking materials for imaging and therapy phantoms: a review. *Physics in Medicine Biology*, 2020. DOI :10.1088/1361-6560/abbd17.

[38] David Frederick Pepley, Cheyenne Cassel Sonntag, Rohan Sunil Prabhu, Mary Alice Yovanoff, David C. Han, Scarlett Rae Miller, and Jason Zachary Moore. Building ultrasound phantoms with modified polyvinyl chloride: A comparison of needle insertion forces and sonographic appearance with commercial and traditional simulation materials. *Simulation in Healthcare: The Journal of the Society for Simulation in Healthcare*, 2018. DOI: 10.1097/SIH.0000000000000302.

[39] Y.L. Liao, H.B. Chen, L.H. Zhou, and X. Zhen. Construction of an anthropopathic abdominal phantom for accuracy validation of deformable image registration. *Technology and Health Care*, 2016. DOI: 10.3233/THC-161200.

[40] J. Fromageau, J.-L. Gennisson, C. Schmitt, R.L. Maurice, R. Mongrain, and G. Cloutier. Estimation of polyvinyl alcohol cryogel mechanical properties with

four ultrasound elastography methods and comparison with gold standard testings. *IEEE Transactions on Ultrasonics, Ferroelectrics and Frequency Control*, 2007. DOI : 10.1109/TUFFC.2007.273.

[41] Richard W. Nuckols, Krithika Swaminathan, Sangjun Lee, Louis Awad, Conor J. Walsh, and Robert D. Howe. Automated detection of soleus concentric contraction in variable gait conditions for improved exosuit control. In *2020 IEEE International Conference on Robotics and Automation (ICRA)*. IEEE, 2020. DOI : 10.1109/ICRA40945.2020.9197428.

[42] Dorsiflexion. *919 Spine*. url: https://www.919spine.com/blog/dorsiflexion.

[43] Sion Hwang. Understanding motion estimation using optical flow techniques, 2023. url: https://medium.com/@sharco0212/understanding-motion-estimation-using-optical-flow-techniques-67a41d4c454f.

[44] Chuan en Lin. Introduction to motion estimation with optical flow. *Nanonets AI Machine Learning Blog*, 2019. url : https://nanonets.com/blog/optical-flow/.

[45] David Young. Affine Optic Flow, 2023. MATLAB. url : https://www.mathworks.com/matlabcentral/fileexchange/27093-affine-optic-flow.